NASA CONTRACTOR REPORT

NASA CR-2

ANALYSIS OF ATMOSPHERIC FLOW OVER A SURFACE PROTRUSION USING THE TURBULENCE KINETIC ENERGY EQUATION WITH REFERENCE TO AERONAUTICAL OPERATING SYSTEMS

Walter Frost and W. L. Harper

NATIONAL AERONAUTICS AND SPACE ADMINISTRATION • WASHINGTON, D. C. • DECEMBER 1975

1. REPORT NO. NASA CR- 2630	2. GOVERNMENT ACCESSION NO.	3. RECIPIENT'S CATALOG NO.		
4 TITLE AND SUBTITLE Analysis of Atmospheric Flow Over a Surface Protrusion Using the Turbulence Kinetic Energy Equation With Reference to Aeronautical Operating Systems		5. REPORT DATE December 1975		
		6. PERFORMING ORGANIZATION CODE		
7. AUTHOR(S) Walter Frost and W. L. Harper		8. PERFORMING ORGANIZATION REPORT # M154		
9. PERFORMING ORGANIZATION NAME AND ADDRESS The University of Tennessee Space Institute Tullahoma, Tennessee 37388		10. WORK UNIT NO.		
		11. CONTRACT OR GRANT NO. NAS8-29584		
12. SPONSORING AGENCY NAME AND ADDRESS National Aeronautics and Space Administration Washington, D. C. 20546		13. TYPE OF REPORT & PERIOD COVERED December 1973-December 1974 Contractor		
		14. SPONSORING AGENCY CODE		

15. SUPPLEMENTARY NOTES
This report was prepared under the technical monitorship of the Aerospace Environment Division, Space Sciences Laboratory, NASA/Marshall Space Flight Center.

16. ABSTRACT Flow over surface obstructions can produce significantly large wind shears such that adverse flying conditions can occur for aeronautical systems (helicopters, STOL vehicles, etc.). Atmospheric flow fields resulting from a semi-elliptical surface obstruction in an otherwise horizontally homogeneous statistically stationary flow are modelled with the boundary-layer/Boussinesq-approximation of the governing equation of fluid mechanics. The turbulence kinetic energy equation is used to determine the dissipative effects of turbulent shear on the mean flow. Mean flow results are compared with those of a previous paper where the same problem was attacked using a Prandtl mixing length hypothesis. The diffusion and convection of turbulence kinetic energy not accounted for in the Prandtl mixing length concept cause departures of the mean wind profiles from those previously computed primarily in the regions of strong pressure gradients.

Iso-lines of turbulence kinetic energy and turbulence intensity are plotted in the plane of the flow and highlight regions of high turbulence intensity in the stagnation zone and sharp gradients in intensity along the transition from adverse to favourable pressure gradient.

Discussion of the effects of the disturbed wind field on CTOL and STOL aircraft flight path and obstruction clearance standards is given. The results indicate that closer inspection of these presently recommended standards as influenced by wind over irregular terrains is required.

17. KEY WORDS Wind Shear Aviation Safety Gusts	18. DISTRIBUTION STATEMENT Category 20		
19. SECURITY CLASSIF. (of this report) UNCLASSIFIED	20. SECURITY CLASSIF. (of this page) UNCLASSIFIED	21. NO. OF PAGES 76	22. PRICE $4.25

FOREWORD

The research reported in this document is concerned with the results of
a study of atmospheric boundary layer flow over surface obstacles using
an advance turbulent closure scheme involving the turbulence kinetic energy
equation. It is part of our investigation to determine the wind environments
that are induced by buildings, etc., in the vicinity of airports, heliports,
STOL-ports, etc., relative to assessing and defining the possible hazardous
flying conditions which could result from these wind environments. The last
chapter of the report (Chapter IX) represents an analysis of the implications
of the calculated induced wind environments on aeronautical safety.

TABLE OF CONTENTS

LIST OF FIGURES

NOMENCLATURE

a_1	Proportionality constant of shear stress to turbulence kinetic energy
b	Height of elliptical body
E_o	Reference turbulence kinetic energy
e	Dimensionless turbulence kinetic energy
f	Coriolis parameter
G	Universal function of $z*/\delta$
k	Effective viscosity
L	Mixing length
ℓ	Prandtl mixing length
N	Number of grid points in vertical direction
p	Pressure
Sc_e	Ratio of turbulent eddy viscosity to a coefficient for energy transfer
u	Dimensionless velocity component in x direction
u_*^*	Friction velocity, $\sqrt{\tau/\rho}$
$\hat{u}'$	Turbulence intensity
U_e	Dimensionless velocity along streamline
U_∞	Reference velocity
v	Dimensionless velocity component in y direction
w	Dimensionless velocity component in z direction
x	Dimensionless horizontal coordinate parallel to direction of flow
z	Dimensionless vertical coordinate
α	Aspect ratio of ellipse
γ	Intermittency
δ	Boundary layer thickness

ε	Dissipation term of turbulence kinetic energy equation
ζ	Stretched vertical coordinate
κ	von Karman's constant
λ	Length of separation bubble
ν	Kinematic viscosity
ρ	Density
σ_u	Root mean square value of fluctuating u velocity component
σ_v	Root mean square value of fluctuating v velocity component
σ_w	Root mean square value of fluctuating w velocity component
τ	Turbulent shear stress
υ	Convection velocity
Φ	Vertical coordinate stretching function
ψ	Stream function

Superscripts

$*$	Dimensional quantity
$'$	Turbulent fluctuating component
$(\overline{})$	Ensemble average operator

Subscripts

| o | Initial value from undisturbed upstream flow |

CHAPTER I

INTRODUCTION

The flow fields induced around buildings and other
structures by the surface winds are of considerable impor-
tance with respect to the design of aeronautical facilities,
particularly in the case of helicopter and V/STOL facilities
in metropolitan areas where these aircraft may be operated
from the tops of buildings. Severe updrafts and downdrafts
and regions with high turbulence levels make take-off and
landing of aircraft near buildings hazardous. These hazards
can be attenuated by modifying airport design or aircraft
operation procedures so as to reduce the influence of the
flow fields caused by the wind. This, however, requires
methods for obtaining quantitative descriptions of the
atmospheric flow at the aerodrome.

One method is to measure the flow conditions at
existing aerodromes. This method is impractical because of
the large number of measurements required and the vast
amount of data which would have to be reduced.

The above comments are not meant to suggest that wind
measurements at airports are not required, but that entire
flow field patterns cannot practically be established in
this manner. Measurements with one or two individual masts
could, however, be supplemented with analytical methods
which would allow logical extrapolation of these measure-
ments and thus allow predictions of the overall wind pattern

about the airfield to be made. McManus [1][1] observed that
neither time histories nor rms values measured by aircraft
agree with values determined from an individual mast and
concluded that the turbulence and mean wind pattern seen by
the aircraft was defined by the geometry of the airfield.

Since geometry plays a significant role, it is further
obvious that rather extensive measurements made at one air-
field could not be employed to design few facilities whereas
numerical models would have this flexibility. Moreover,
analytical models of winds about irregular surface geometries
are also of interest to airplane design and flight simulation
(see [2, 3]).

The need of an analytical approach is thus indicated.
A solution of the complete equations of motion for turbulent
flow would provide the desired information but such solu-
tions are not practical because of the great expense of com-
puter time required to achieve results.

The concept of a disturbed boundary layer with turbu-
lence modeled after the Prandtl mixing length hypothesis was
used by Frost, Maus, and Simpson [4] to approximate a
solution of the general equations. The two-dimensional
boundary layer equations were solved for flow over semi-
elliptical cylinders.

The significant conclusions of the above mentioned

---

[1]Numbers in brackets refer to similarly numbered
references in the list of references.

study were:

1. A localized maximum in wind speed is produced at the top of a semi-elliptical body, the maximum velocity increasing with decreasing elliptical aspect ration.

2. Increased surface roughness decreases the wind velocity in the boundary layer.

3. Decreasing elliptical aspect ratio and/or increasing surface roughness cause a larger separation region upstream of the body.

The question of the validity of the Prandtl mixing length theory for atmospheric flow in disturbed regions gives a degree of uncertainty to the above conclusions, however. Moreover, this method of solution does not give any information about the turbulence structure of the flow field.

The purpose of this report is to develop solutions which will shed light on the validity of the results obtained from the Prandtl mixing length hypothesis. Flow fields are calculated with the boundary layer equations using equivalent boundary conditions employed in [4], but with the equation of conservation of turbulence kinetic energy used to model the turbulence kinetic energy statistics. If the flow fields predicted by the two methods of solution do not differ significantly, then both models can be employed with greater confidence. Of the two methods of solutions, the Prandtl mixing length method has the advantage of requiring less computation time, whereas, the turbulence kinetic energy method has the advantage of allowing for the

3

turbulence to feed from the mean flow via the energy equation giving physically more meaningful values of turbulence intensity levels.

The method developed in this study can be applied to flow over very general two-dimensional bodies, however, for the purposes of comparison with the method of Frost, Maus, and Simpson [4], the solutions presented will be limited to semi-elliptical cylinders with various aspect ratios and surface roughnesses.

CHAPTER II

TURBULENCE KINETIC ENERGY MODELS

The equation of conservation of turbulence kinetic energy is employed to close the equations of continuity and conservation of momentum. In order to achieve closure, a relationship between the turbulence kinetic energy and the turbulent shear stress is hypothesized. Byrne [5], Lee and Harsha [7], and Bradshaw, Ferris, and Atwell [7] have proposed the relationship,

$$\frac{\tau}{\rho} = a_1 e^* \frac{\partial u^*}{\partial z^*} \left| \frac{\partial u^*}{\partial z^*} \right|^{-1} \tag{1}$$

where τ is the turbulent shear stress,

$$\tau = -\rho \overline{u'w'}$$

e^* is the turbulence kinetic energy,

$$e^* = \frac{1}{2}(\overline{u'^2} + \overline{v'^2} + \overline{w'^2}) \tag{2}$$

and a_1 is a "universal" constant.

For a neutral atmosphere, it has been experimentally determined, as reported by Fichtl [5], that:

$$\left(\frac{\sigma_u}{u^*_*}\right) = 2.5$$

$$\left(\frac{\sigma_v}{u^*_*}\right) = 2.0$$

5

$$\left(\frac{\sigma_w}{u_*}\right) = 1.3$$

where

$$\sigma_u = (\overline{u'^2})^{1/2}$$

$$\sigma_v = (\overline{v'^2})^{1/2}$$

$$\sigma_w = (\overline{w'^2})^{1/2}$$

and

$$u_*^* = \sqrt{\tau/\rho} \tag{3}$$

Therefore,

$$e_* = \frac{1}{2}(\overline{u'^2} + \overline{v'^2} + \overline{w'^2})$$

$$= \frac{1}{2}u_*^{*2}\left[\left(\frac{\sigma_u}{u_*}\right)^2 + \left(\frac{\sigma_v}{u_*}\right)^2 + \left(\frac{\sigma_w}{u_*}\right)^2\right]$$

$$\simeq 6\ u_*^{*2}$$

This result is strictly valid for a horizontally homogeneous neutrally stratified boundary layer; however, we shall assume that it also hold for turbulent flow over an obstruction. Thus, from Equation 1, for a neutral atmosphere, $a_1 \simeq 1/6$.

The steady state turbulence kinetic energy equation is (in tensor notation) from Harsha [9]:

$$u_i^* \frac{\partial e^*}{\partial x_i^*} = -\overline{u_i' u_j'} \frac{\partial u_j^*}{\partial x_i^*} - \nu \left(\overline{\frac{\partial u_j'}{\partial x_i^*}}\right)^2$$

Convection   Production   Dissipation

$$- \left\{ \frac{\partial}{\partial x_i^*} \overline{[u_i'(p/\rho + e^{*'})]} - \nu \frac{\partial^2 e}{\partial x_i^{*2}} \right\} \tag{4}$$

Diffusion

The production term represents the production of turbulence kinetic energy by the working of the flow against the turbulent stresses $\tau = -\rho \overline{u_i' u_j'}$.

The diffusion term is composed of the gain of energy by flow down pressure gradients, $-\partial(\overline{u_i'\, p/\rho})/\partial x_i^*$, the transport of turbulence energy by large eddies, $-\partial(\overline{u_i'\, e^{*'}})/\partial x_i^*$, and a gradient-diffusion term $\nu \partial^2 e^*/\partial x_i^{*2}$. If the gradient diffusion term is considered to be negligible compared to the convective diffusion term, the resulting turbulence energy budget, with the continuity and momentum equations, gives a hyperbolic system of equations. Bradshaw, Ferris, and Atwell [7] neglect the gradient diffusion term and use as a diffusion term, $\partial(a_1 e^* \upsilon)/\partial z^*$ where υ is a convection velocity defined by,

$$\upsilon \equiv \left(\frac{\tau_{max}}{\rho}\right)^{1/2} G(z^*/\delta)$$

with G modeled from experimental data as:

$$G = \left[\overline{\left(w' \frac{p'}{\rho}\right)} + \overline{w' e^{*'}} \right] \Big/ \left[\left(\frac{\tau_{max}}{\rho}\right)^{1/2} \tau/\rho \right]$$

7

where τ_{max} is the maximum shear stress across the velocity profile and δ is the boundary layer thickness. The resulting hyperbolic system of three equations is solved by the method of characteristics.

While the solution of a hyperbolic system of three equations may require less computer time than a parabolic system, the complexity of the hyperbolic solution increases greatly if additional equations such as species or total energy equations are added to the system. References [9, 6, 5] incorporate a gradient diffusion term, $\partial\left(\dfrac{k}{Sc_e}\dfrac{\partial e^*}{\partial z^*}\right)/\partial z^*$ where k is an effective viscosity defined by,

$$k \equiv \frac{|\tau|}{\rho\,|\partial u^*/\partial z^*|} \tag{5}$$

The symbol Sc_e is an effective Schmidt number which represents the ratio of turbulent eddy viscosity to a diffusion coefficient for energy.

The resulting turbulence kinetic energy equation is parabolic and can be solved simultaneously with the momentum and continuity equations.

This latter approach is also applicable in this study since the primary interest lies in the lower portion of the atmospheric boundary layer where the average eddy size is small compared to that in the upper region of the boundary layer, and hence the magnitude of the convective diffusion term is small compared to the production and dissipation terms [10]. Consequently, the gradient diffusion term is

used in order to simplify the solution of the equations.

An approximation must be made for the dissipation term, $\varepsilon = \nu \overline{(\partial u^*_j / \partial x^*_i)}^2$, in order to obtain a form suitable for computation. Byrne and Lee [11] propose a dissipation term,

$$\varepsilon = (a_2 e^{*3/2})/\delta$$

where δ is the boundary layer thickness, and a_2 is a parameter dependent upon the location of the maximum shear stress, τ_{max}. This dissipation term, however, does not satisfy the condition of constant shear stress which exists for atmospheric boundary layers over flat terrain.

Bradshaw and Ferris [7] propose that,

$$\varepsilon = u_*^{*3}/L \qquad (6)$$

where,

$$u_*^* = \sqrt{\tau/\rho} = (a_1 e^*)^{3/2}$$

and

$$L = \begin{cases} \kappa z^*, & \text{near the surface} \\ 0.095\gamma^{1/2}, & \text{in outer layer} \end{cases}$$

where κ is the von Karman constant, and γ is the intermittency.

It can be shown that for steady flow with no pressure gradient, corresponding to a logarithmic velocity profile where production equals dissipation, the dissipation term is

given by,

$$\varepsilon = \frac{u_*^{*3}}{\kappa(z^* + z_o^*)} \tag{7}$$

where z_o^* is the surface roughness height. Thus, ε satisfies the initial upstream condition of a logarithmic approaching velocity profile. For $z^* >> z_o^*$, the value of ε given by (7) is approximately equal to that given by (6). Therefore (7) has been chosen for the dissipation function in this report. This dissipation function is valid far upstream, but whether it applies in the vicinity of the body is not known and must eventually be established by experiment.

The Governing Equations

The equations of motion for steady, incompressible flow within the atmospheric boundary layer are well established [4, 12]. The continuity equation is:

$$\frac{\partial u^*}{\partial x^*} + \frac{\partial w^*}{\partial z^*} = 0 \tag{8}$$

The longitudinal momentum equation is:

$$u^* \frac{\partial u^*}{\partial x^*} + w^* \frac{\partial u^*}{\partial z^*} = -1/\rho \frac{\partial p}{\partial x^*} + \frac{\partial}{\partial z^*} \tau_{xz} + fv^* \tag{9}$$

where f is the Coriolis parameter.

Below a height of about 50 m the apparent force produced by the Coriolis effect due to the Earth's rotation is negligible compared to the vertical gradient in τ_{xz} [4], so the term fv^* can be omitted from (9).

Based on the approximations made for the diffusion and dissipation terms, the turbulence kinetic energy equation for steady, two-dimensional flow is,

$$u^* \frac{\partial e^*}{\partial x^*} + w^* \frac{\partial e^*}{\partial z^*} = \frac{\partial}{\partial z^*}\left[\frac{k}{Sc_e}\frac{\partial e^*}{\partial z^*}\right] + \frac{\tau}{\rho}\frac{\partial u^*}{\partial z^*} - \frac{u_*^{*3}}{\kappa(z^* + z_o^*)}. \qquad (10)$$

Substituting Equations (1), (3), and (5) into (9) and (10), the governing equations become:

Continuity,

$$\frac{\partial u^*}{\partial x^*} + \frac{\partial w^*}{\partial z^*} = 0 \qquad (11)$$

Momentum,

$$u^* \frac{\partial u^*}{\partial x^*} + w^* \frac{\partial u^*}{\partial z^*} = - \frac{1}{\rho}\frac{\partial p}{\partial x^*} + \frac{\partial}{\partial z^*}\left[\frac{a_1 e^*}{|\partial u^*/\partial z^*|}\frac{\partial u^*}{\partial z^*}\right] \qquad (12)$$

Turbulence Kinetic Energy,

$$u^* \frac{\partial e^*}{\partial x^*} + w^* \frac{\partial e^*}{\partial z^*} = \frac{\partial}{\partial z^*}\left[\frac{a_1 e^*}{Sc_e|\partial u^*/\partial z^*|}\frac{\partial e^*}{\partial z^*}\right] + \frac{a_1 e^*}{|\partial u^*/\partial z^*|}\left(\frac{\partial u^*}{\partial z^*}\right)^2$$

$$- \frac{(a_1 e^*)^{3/2}}{\kappa(z^* + z_o^*)} \qquad (13)$$

CHAPTER III

NUMERICAL SOLUTION OF THE GOVERNING EQUATIONS

The continuity, momentum, and turbulence kinetic energy equations form a closed set of nonlinear, parabolic partial differential equations given by Equations (11), (12), and (13). The boundary conditions for these equations are: $u^* = 0$, $e^* = u_{*_0}^{*2}/a_1$, at $z^* = 0$, and $u^* = u_{log}^*(z_{max}^*)$, $e^* = E_o$, at $z^* = z_{max}^*$ where E_o is the turbulence kinetic energy corresponding to a logarithmic velocity profile, z_{max} is a height above which the influence of the body is assumed negligible, and $u_{log}^*(z_{max}^*)$ is the velocity at height z_{max}^* corresponding to a logarithmic velocity profile. The equations are solved numerically by the procedure described below.

The pressure gradient term in Equation (12) is approximated by the pressure distribution of the inviscid solution for flow over an ellipse [4]. The pressure distribution used corresponds to the streamline nearest to the body which allows stable solutions of the momentum and turbulence kinetic energy equations to the top of the ellipse. This "non-separating" streamline is determined by iteratively introducing streamlines further and further from the body until a pressure distribution which permits a complete, stable solution is found. Jackson and Hunt [13] have, through a perturbation analysis, analytically confirmed the validity of this pressure distribution for the outer layer

12

of the flow field over a surface hump. (See also Reference [4].) From Bernoulli's equation:

$$- \frac{1}{\rho} \frac{dp}{dx^*} = U^*_e \frac{dU^*_e}{dx^*} \qquad (14)$$

the pressure gradient term in Equation (12) can be expressed in terms of U^*_e, which is the velocity given by the potential flow solution along the non-separating streamline.

Adopting a characteristic length b, equal to the height of the ellipse, a characteristic velocity U_∞, equal to $(u_*/\kappa) \ln (3b + z^*_o)/z^*_o$ for the initial velocity profile, and a characteristic turbulence kinetic energy E_o, equal to u_*^2/a_1 for the initial turbulence kinetic energy profile, the governing equations can be expressed in the following non-dimensional form,

$$\frac{\partial u}{\partial x} + \frac{\partial w}{\partial z} = 0 \qquad (15)$$

$$u \frac{\partial u}{\partial x} + w \frac{\partial u}{\partial z} = U_e \frac{dU_e}{dx} + \frac{a_1 E_o}{U_\infty^2} \frac{\partial}{\partial z} \left(\frac{e}{|\partial u/\partial z|} \frac{\partial u}{\partial z} \right) \qquad (16)$$

$$u \frac{\partial e}{\partial x} + w \frac{\partial e}{\partial z} = \frac{a_1 E_o}{Sc_e U_\infty^2} \frac{\partial}{\partial z} \left(\frac{e}{|\partial u/\partial z|} \frac{\partial e}{\partial z} \right) + a_1 e \left| \frac{\partial u}{\partial z} \right|$$

$$- \frac{a_1^{3/2} E_o^{1/2}}{\kappa U_\infty} \frac{e^{3/2}}{(z + z_o)} \qquad (17)$$

where:

$e = e^*/E_o$

$u = u^*/U_\infty$

13

$$w = w*/U_\infty$$

$$U_e = U_e^*/U_\infty$$

$$x = x*/b$$

$$z = z*/b$$

$$z_o = z_o^*/b$$

In the finite difference scheme used to solve the governing equations, it is advantageous to transform the vertical coordinate in order to compress the vertical length scale near the surface such that more grid points will occur in the region where the velocity gradients are most severe. The transformation is in the form of a stretching function $\zeta = f(z)$. Applying the transformation to the vertical derivative results in the relationship:

$$\frac{\partial}{\partial z} = f'(z) \frac{\partial}{\partial \zeta}$$

Defining the function,

$$\Phi(\zeta) \equiv f'(z) = f'[g(\zeta)]$$

the governing equations become:

Continuity,

$$\frac{\partial u}{\partial x} + \Phi \frac{\partial w}{\partial \zeta} = 0 \tag{18}$$

Momentum,

$$u \frac{\partial u}{\partial x} + w\Phi \frac{\partial u}{\partial \zeta} = U_e \frac{dU_e}{dx} + \frac{a_1 E_o}{U_\infty^2} \Phi \frac{\partial}{\partial \zeta}\left[\frac{\Phi}{|\Phi|} \frac{e}{|\partial u/\partial \zeta|} \frac{\partial u}{\partial \zeta}\right] \tag{19}$$

14

Turbulence Kinetic Energy,

$$u \frac{\partial e}{\partial x} + \Phi w \frac{\partial e}{\partial \zeta} = \frac{a_1 E_o}{Sc_e U_\infty^2} \Phi \frac{\partial}{\partial \zeta}\left[\frac{\Phi}{|\Phi|} \frac{e}{|\partial u/\partial \zeta|} \frac{\partial e}{\partial \zeta}\right] + a_1 |\Phi| \ e \left|\frac{\partial u}{\partial \zeta}\right|$$

$$- \frac{a_1^{3/2} E_o^{1/2}}{\kappa \ U_\infty} \frac{e^{3/2}}{(z + z_o)} \tag{20}$$

Finite Difference Form

The preceding equations are solved by an implicit, finite difference technique. The flow field over the cylinder is assumed to be represented by Cartesian grid system shown in Figure 1. Curvature effects are assumed negligible since the flow field within the stagnation regions has already been neglected by the assumption that the pressure distribution imposed on the flow is given by that along the non-separating streamline [4]. The equations of motion can be solved by approximating the derivatives with finite difference forms expressed in terms of nodal points of the grid. This approximation results in a set of equations involving the unknown values at an x-station m+1 and known values at x-station m. The derivatives of the u velocity component are expressed as:

$$\left.\frac{\partial u}{\partial x}\right|_{m+1,n} = \frac{u_{m+1,n} - u_{m,n}}{\Delta x}$$

$$\left.\frac{\partial u}{\partial \zeta}\right|_{m+1,n} = \frac{u_{m+1,n+1} - u_{m+1,n-1}}{2\Delta \zeta}$$

z,Z

(a) PHYSICAL COORDINATES

x,X

z

n + 1

n

n - 1

x

m   m + 1

(b) ASSUMED NUMERICAL COORDINATES

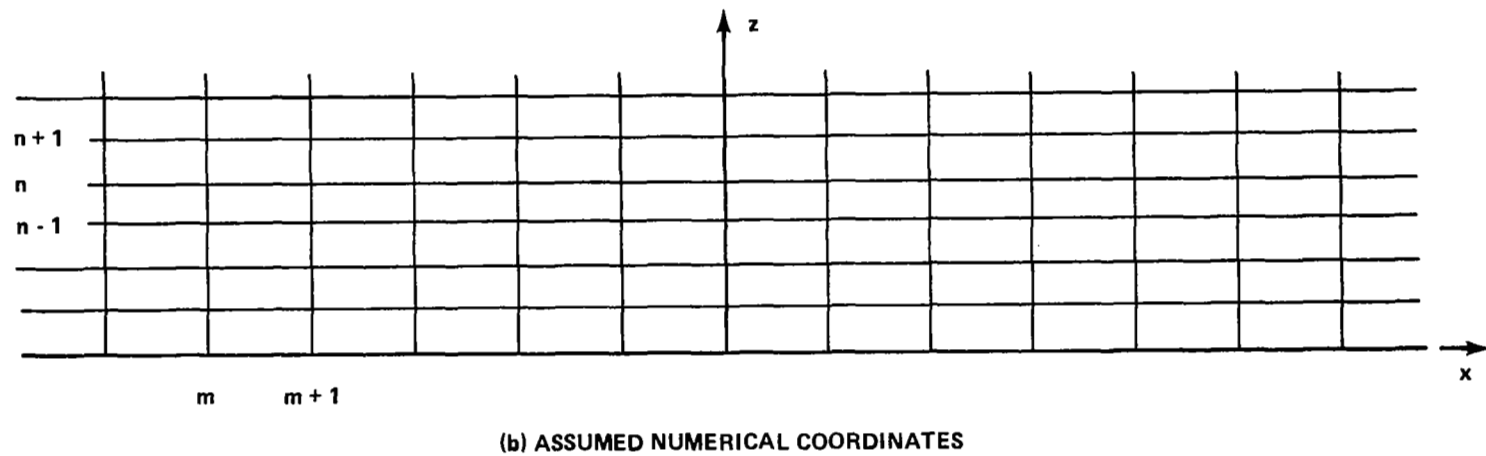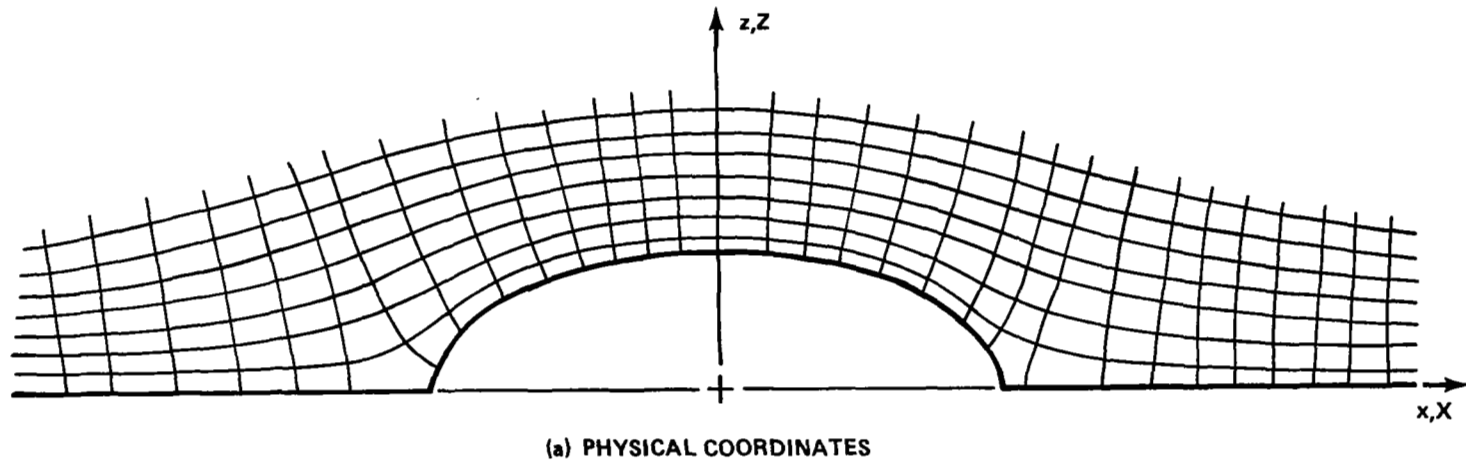Figure 1.   Coordinate System Over the Elliptical Cylinder

$$\left.\frac{\partial^2 u}{\partial \zeta^2}\right|_{m+1,n} = \frac{u_{m+1,n+1} - 2u_{m+1,n} + u_{m+1,n-1}}{(\Delta \zeta)^2}$$

The derivatives of the other variables are expressed simi-
larly. Since the momentum and turbulence kinetic energy
equations are nonlinear, an iterative procedure must be
introduced into the numerical scheme.

The finite difference equations are made linear by
replacing the dependent variables which appear to powers
other than the first by a factored product of the variable
to the first power and the remainder which is approximated
with values of the variable from the previous iteration.
For the first iteration at an x-station m+1, the known
values of the variable (u or e) at station m are used to
linearize the equations. The system is solved at m+1, and
this solution is used to linearize the equations for the
second iteration. This procedure is repeated until the
desired degree of convergence is attained. The method is
then repeated at m+2 using the solution at m+1 to initially
linearize the equations. In this way the numerical pro-
cedure marches downstream.

The solution procedure is initiated at a prescribed
distance upstream with a logarithmic velocity profile. The
initial turbulence kinetic energy profile is obtained by
iterating on e with the logarithmic u profile fixed. The
solution procedure then advances to the first x-station.

The first step in the iteration loop is to solve the

17

momentum equation for u, using values of e obtained from the previous iteration, or in the case of the first iteration at m+1, from the solution at m. The momentum equation, Equation (19), is repeated here for convenience.

$$u \frac{\partial u}{\partial x} + w\Phi \frac{\partial u}{\partial \zeta} = U_e \frac{dU_e}{dx} + \frac{a_1 E_o}{U_\infty^2} \Phi \frac{\partial}{\partial \zeta} \left[\frac{\Phi}{|\Phi|} \frac{e}{|\partial u/\partial \zeta|} \frac{\partial u}{\partial \zeta} \right]$$

Note that the last term on the right side can be written,

$$\frac{a_1 E_o}{U_\infty^2} |\Phi| A \frac{\partial e}{\partial \zeta}$$

where,

$$A = \frac{\partial u/\partial \zeta}{|\partial u/\partial \zeta|} = \begin{cases} +1, & \partial u/\partial \zeta > 0 \\ -1, & \partial u/\partial \zeta < 0 \end{cases}$$

Since

$$\frac{\Phi}{|\Phi|} = \begin{cases} +1, & \Phi > 0 \\ -1, & \Phi < 0 \end{cases}$$

$$\Phi \frac{\partial}{\partial \zeta} \left[\frac{\Phi}{|\Phi|} e \right] = |\Phi| \frac{\partial e}{\partial \zeta}$$

The finite difference form of the momentum equation is then,

$$u_{m+1,n}^T \frac{u_{m+1,n} - u_{m,n}}{\Delta x} + \Phi_n w_{m+1,n}^T \frac{u_{m+1,n+1} - u_{m+1,n-1}}{2\Delta \zeta}$$

$$= \left(U_e \frac{dU_e}{dx} \right)_{m+1} + \frac{a_1 E_o}{U_\infty^2} |\Phi_n| A \left(\frac{e_{m+1,n+1}^T - e_{m+1,n-1}^T}{2\Delta \zeta} \right) \quad (21)$$

where the superscript T denotes a trial value from the previous iteration.

18

Rearranging terms, we obtain,

$$\left(\frac{\Phi_n w^T_{m+1,n}}{2} \frac{\Delta x}{\Delta \zeta}\right) u_{m+1,n+1} + (u^T_{m+1,n}) u_{m+1,n}$$

$$+ \left(-\frac{\Phi_n w^T_{m+1,n}}{2} \frac{\Delta x}{\Delta \zeta}\right) u_{m+1,n-1} = \left(U_e \frac{dU_e}{dx}\right)_{m+1} \Delta x$$

$$+ \frac{a_1 E_o}{U^2_\infty} A|\Phi_n| \left(\frac{e^T_{m+1,n+1} - e^T_{m+1,n-1}}{2}\right) \frac{\Delta x}{\Delta \zeta} + u^T_{m+1,n} u_{m,n} \quad (22)$$

which has the form,

$$A_n u_{m+1,n+1} + B_n u_{m+1,n} + C_n u_{m+1,n-1} = D_n, \quad (2 \leq n \leq N - 1)$$
$$\hspace{10cm} (23)$$

where N is the number of nodal points at m+1, and

$$A_n = \frac{\Phi_n w^T_{m+1,n}}{2} \frac{\Delta x}{\Delta \zeta}$$

$$B_n = u^T_{m+1,n}$$

$$C_n = -A_n$$

$$D_n = \left(U_e \frac{dU_e}{dx}\right)_{m+1} \Delta x + \frac{a_1 E_o}{U^2_\infty} A|\Phi_n| \left(\frac{e^T_{m+1,n+1} - e^T_{m+1,n-1}}{2}\right) \frac{\Delta x}{\Delta \zeta}$$

$$+ u^T_{m+1,n} u_{m,n}$$

Applying these equations at each of the nodal points between the surface and outer boundary results in a system of N - 2 algebraic equations which yield a tridiagonal coefficient matrix which can be solved by the following

recursion formula:

$$u_{m+1,n} = E_n u_{m+1,n+1} + F_n$$

and,

$$u_{m+1,n-1} = E_{n-1} u_{m+1,n} + F_{n-1} \qquad (24)$$

Substituting into Equation (23),

$$A_n u_{m+1,n+1} + B_n u_{m+1,n} + C_n [E_{n-1} u_{m+1,n} + F_{n-1}] = D_n$$

and solving for $u_{m+1,n}$

$$u_{m+1,n} = \frac{-A_n u_{m+1,n+1}}{B_n + C_n E_{n-1}} + \frac{D_n - C_n F_{n-1}}{B_n + C_n E_{n-1}}$$

which means,

$$E_n = -\frac{A_n}{B_n + C_n E_{n-1}} \qquad (25)$$

$$F_n = \frac{D_n - C_n F_{n-1}}{B_n + C_n E_{n-1}} \qquad (26)$$

Boundary Conditions on u

The inner boundary condition of no slip at the ground in Equation (24) gives E_1 and F_1 as zero. Equations (25) and (26) are used to calculate the E_n's and F_n's from $n = 2$ outward to $n = N - 1$. The outer boundary condition,

20

$$u_{m+1,N} = \frac{u_*}{\kappa} \ln\left(\frac{6.3 + z_o}{z_o}\right)$$

which was chosen based on computational experience with the program, is used in Equation (24) to begin calculation of the u_n's from $n = N - 1$ inward to $n = 2$.

The velocity profile in the vertical direction is solved by integrating the continuity equation, Equation (18),

$$w(\zeta) = -\int_o^\zeta \left(\frac{\partial u}{\partial x}\right) \left(\frac{1}{\Phi}\right) d\zeta$$

Approximating the integral by the trapezoidal rule, the vertical velocity is calculated outward from the surface with,

$$w_{m+1,n} = w_{m+1,n-1} - \frac{\Delta\zeta}{2}\left(\frac{1}{\Phi_{n-1}} \frac{u_{m+1,n-1} - u_{m,n-1}}{\Delta x}\right.$$
$$\left. + \frac{1}{\Phi_n} \frac{u_{m+1,n} - u_{m,n}}{\Delta x}\right) \tag{27}$$

We now direct attention to the turbulence kinetic energy equation, Equation (20), which is repeated here for convenience,

$$u \frac{\partial e}{\partial x} + \Phi w \frac{\partial e}{\partial \zeta} = \frac{a_1 E_o}{Sc_e U_\infty^2} \Phi \frac{\partial}{\partial \zeta}\left(\frac{\Phi}{|\Phi|} \frac{e}{|\partial u/\partial \zeta|} \frac{\partial e}{\partial \zeta}\right) + a_1|\Phi| e \left|\frac{\partial u}{\partial \zeta}\right|$$
$$- \frac{a_1^{3/2} E_o^{1/2}}{\kappa U_\infty} \frac{e^{3/2}}{(z + z_o)}$$

The finite difference form of the equation is

$$u^T_{m+1,n} \frac{e_{m+1,n} - e_{m,n}}{\Delta x} + \Phi_n \, w^T_{m+1,n} \frac{e_{m+1,n+1} - e_{m+1,n-1}}{2\Delta\zeta}$$

$$= \frac{a_1 E_o}{Sc_e U^2_\infty} |\Phi_n| \left[\left(\frac{e_{m+1,n+1} - e_{m+1,n-1}}{2\Delta\zeta} \right)^2 \left| \frac{2\Delta\zeta}{u^T_{m+1,n+1} - u^T_{m+1,n-1}} \right| \right.$$

$$+ e_{m+1,n} \left(\frac{e_{m+1,n+1} - 2e_{m+1,n} + e_{m+1,n-1}}{(\Delta\zeta)^2} \right)$$

$$\left| \frac{2\Delta\zeta}{u^T_{m+1,n+1} - u^T_{m+1,n-1}} \right| - e_{m+1,n} \left(\frac{e_{m+1,n+1} - e_{m+1,n-1}}{2\Delta\zeta} \right)$$

$$\left| \frac{2\Delta\zeta}{u^T_{m+1,n+1} - u^T_{m+1,n-1}} \right|^2 \left\{ \frac{|u^T_{m+1,n+1} - u^T_{m+1,n}|}{(\Delta\zeta)^2} \right.$$

$$\left. \left. - \frac{|u^T_{m+1,n} - u^T_{m+1,n-1}|}{(\Delta\zeta)^2} \right\} \right] + a_1 |\Phi_n| \, e_{m+1,n}$$

$$\left| \frac{u^T_{m+1,n+1} - u^T_{m+1,n-1}}{2\Delta\zeta} \right| - \frac{a_1^{3/2} E_o^{1/2} e^{T^{1/2}}_{m+1,n}}{\kappa \, U_\infty} \frac{e_{m+1,n}}{(z + z_o)} \qquad (28)$$

Rearranging terms, Equation (28) can be written as,

$$G_n e_{m+1,n+1} + H_n e_{m+1,n} + I_n e_{m+1,n-1} = J_n, \quad (2 \le n \le N - 1) \qquad (29)$$

where,

$$G_n = \frac{\Phi_n \, w^T_{m+1,n}}{2} \frac{\Delta x}{\Delta \zeta} - \frac{a_1 E_o \, |\Phi_n|}{Sc_e \, U_\infty^2} \left\{ \frac{e^T_{m+1,n+1} - 2e^T_{m+1,n} + e^T_{m+1,n-1}}{(2\Delta \zeta)^2} \right.$$

$$\left| \frac{2\Delta \zeta}{u^T_{m+1,n+1} - u^T_{m+1,n-1}} \right| + \frac{e^T_{m+1,n}}{(\Delta \zeta)^2} \left| \frac{2\Delta \zeta}{u^T_{m+1,n+1} - u^T_{m+1,n-1}} \right|$$

$$- \frac{e^T_{m+1,n}}{2} \left| \frac{2\Delta \zeta}{u^T_{m+1,n+1} - u^T_{m+1,n-1}} \right|^2$$

$$\left. \left(\frac{|u^T_{m+1,n+1} - u^T_{m+1,n}|}{(\Delta \zeta)^2} - \frac{|u^T_{m+1,n} - u^T_{m+1,n-1}|}{(\Delta \zeta)^2} \right) \right\} \Delta x$$

$$H_n = u^T_{m+1,n} - \frac{a_1 E_o \, |\Phi_n|}{Sc_e \, U_\infty^2} \left\{ - \frac{2e^T_{m+1,n}}{(\Delta \zeta)^2} \left| \frac{2\Delta \zeta}{u^T_{m+1,n+1} - u^T_{m+1,n-1}} \right| \right\} \Delta x$$

$$- a_1 |\Phi_n| \left| \frac{u^T_{m+1,n+1} - u^T_{m+1,n-1}}{2\Delta \zeta} \right| \Delta x$$

$$+ \frac{a_1^{3/2} (E_o e^T_{m+1,n})^{1/2}}{\kappa \, U_\infty} \frac{\Delta x}{(z + z_o)}$$

$$I_n = - \frac{\Phi_n w^T_{m+1,n}}{2} \frac{\Delta x}{\Delta \zeta} - \frac{a_1 E_o |\Phi_n|}{Sc_e \, U_\infty^2} \left\{ \frac{e^T_{m+1,n-1}}{(2\Delta \zeta)^2} \left| \frac{2\Delta \zeta}{u^T_{m+1,n+1} - u^T_{m+1,n-1}} \right| \right.$$

$$+ \frac{e^T_{m+1,n}}{(\Delta \zeta)^2} \left| \frac{2\Delta \zeta}{u^T_{m+1,n+1} - u^T_{m+1,n-1}} \right|$$

$$+ \frac{e^T_{m+1,n}}{2\Delta \zeta} \left| \frac{2\Delta \zeta}{u^T_{m+1,n+1} - u^T_{m+1,n-1}} \right|^2$$

$$\left. \left(\frac{|u^T_{m+1,n+1} - u^T_{m+1,n}| - |u^T_{m+1,n} - u^T_{m+1,n-1}|}{(\Delta \zeta)^2} \right) \right\} \Delta x$$

23

$$J_n = e_{m,n} \, u^T_{m+1,n}$$

As with Equations (23), Equations (29) form a system of N - 2 equations which yield a tridiagonal coefficient matrix which can be solved by the formula,

$$e_{m+1,n-1} = K_{n-1} \, e_{m+1,n} + L_{n-1} \tag{30}$$

where,

$$K_n = - \frac{G_n}{H_n + I_n \, K_{n-1}} \tag{31}$$

$$L_n = \frac{J_n - I_n \, L_{n-1}}{H_n + I_n \, K_{n-1}} \tag{32}$$

Boundary Conditions on e

The inner boundary condition on e is,

$$e_{m+1,1} = \frac{|\tau_w|}{a_1 \, \rho} \frac{U^2_\infty}{E_O} = \frac{(u_{*m+1,1})^2}{a_1} \frac{U^2_\infty}{E_O}$$

where,

$$u_{*m+1,1} = \frac{\kappa \, u_{m+1,2}}{\ln[(z_2 + z_o)]z_o} \tag{33}$$

which assumes that the logarithmic law is obeyed at the wall. Substituting into Equation (30) gives,

$$K_1 = 0$$

$$L_1 = \frac{(u_{*m+1,1} \, U_\infty)^2}{a_1 E_o}$$

Equations (31) and (32) are used to calculate the K_n's and L_n's outward from $n = 2$ to $n = N - 1$. The outer boundary value of $e = 1.0$ is that for an undisturbed boundary layer at the same height above the surface. This boundary condition is used in Equation (30) to begin calculation of the e_n's inward from $n = N$ to $n = 1$.

In summary, the procedure for calculating the u and w velocity profiles and turbulence kinetic energy profile at m+1 is:

1. Calculate A_n, B_n, C_n, and D_n from known values.

2. Calculate E_n and F_n by Equations (25) and (26) from $n = 1$ to $n = N - 1$, starting with $E_1 = F_1 = 0$.

3. Calculate $U_{m+1,n}$ inward from the outer boundary condition to $n = 2$ from Equation (23).

4. Calculate $w_{m+1,n}$ in steps from the inner boundary condition $w_1 = 0$ to the outer edge by Equation (27).

5. Calculate G_n, H_n, I_n, J_n from prescribed values.

6. Calculate K_n and L_n by Equations (31) and (32) from $n = 1$ to $n = N - 1$, starting with $K_1 = 0$, $L_1 = (u_{*m+1,1} \, U_\infty)^2 / a_1 E_o$.

7. Calculate $e_{m+1,n}$ inward from $n = N$ to $n = 1$ by Equation (30) with $e_{m+1,N} = (u_{*O} U_\infty)^2 / a_1 E_o$ for the undisturbed boundary layer.

25

8. Return to step 1 using newly calculated u, w, and e profiles, and repeat procedure until desired convergence is attained.

Convergence

The convergence of the numerical scheme given above is strongly affected by the magnitude of the pressure gradient. In order to minimize computational time, a variable step size in the x-direction, was incorporated. The step size is adjusted such that larger values of Δx occur in regions of small pressure gradient and smaller values in regions of large pressure gradient. A step size determined by,

$$\Delta x \propto \left| U_e \frac{dU_e}{dx} \right|^{-1/2}$$

has been found to give satisfactory results.

Convergence criteria established in Reference [4] for grid spacing Δx, and $\Delta \zeta$ to assure convergence of the iteration process and to minimize truncation error were also observed.

CHAPTER IV

RESULTS AND DISCUSSION

Numerical solutions of the governing equations have been carried out for elliptical cylinders with aspect ratios (length of semi-major axis divided by the height of cylinder) of 2/1, 4/1, and 10/1. The results of these calculations and comparison with a previous solution of the conttinuity and momentum equations based on an eddy viscosity model [4] are presented.

The calculation procedure described previously is initiated with the logarithmic velocity profile character-istic of the approaching wind at a distance sufficiently far upstream of the body that the pressure disturbance created by the body is negligible compared to the free stream pressure. Marching downstream, the velocity profiles are calculated using $u = u_{*_0} \ln[(6.3 + z_0)/z_0]/\kappa$ as the upper bounding condition.

The parameters affecting the solution are the aspect ratio of the elliptical body, α, and the surface roughness of the upstream terrain, z_0, (z_0 is assumed the same for the body).

27

CHAPTER V

COMPARISON OF TURBULENCE KINETIC ENERGY MODEL

WITH PRANDTL MIXING LENGTH MODEL

Velocity profiles calculated by the turbulence kinetic energy (TKE) model with $a_1 = 1/6$ and the Prandtl mixing length (PML) model of [4], are shown in Figures 2, 3, and 4. The flow velocities calculated by the TKE model lag those calculated by the PML model in the adverse pressure gradient region. In the region of favorable pressure gradient, the TKE model velocities overshoot the PML model velocities at some locations and undershoot them at others.

The above observations can be explained by the fact that the mixing length model implies the diffusion and convection terms of the turbulence kinetic energy equation are negligible [14]. One can see this by setting the convection and diffusion terms equal to zero in Equation (10), the turbulence kinetic energy equation then becomes:

$$\frac{\tau}{\rho} \frac{\partial u^*}{\partial z^*} = \frac{u_*^{*3}}{\kappa (z^* + z_o^*)}$$

where,

$$u_*^* = \sqrt{\tau/\rho}$$

Thus,

$$\tau = \rho \ell^2 \left| \frac{\partial u^*}{\partial z^*} \right| \left(\frac{\partial u^*}{\partial z^*} \right)$$
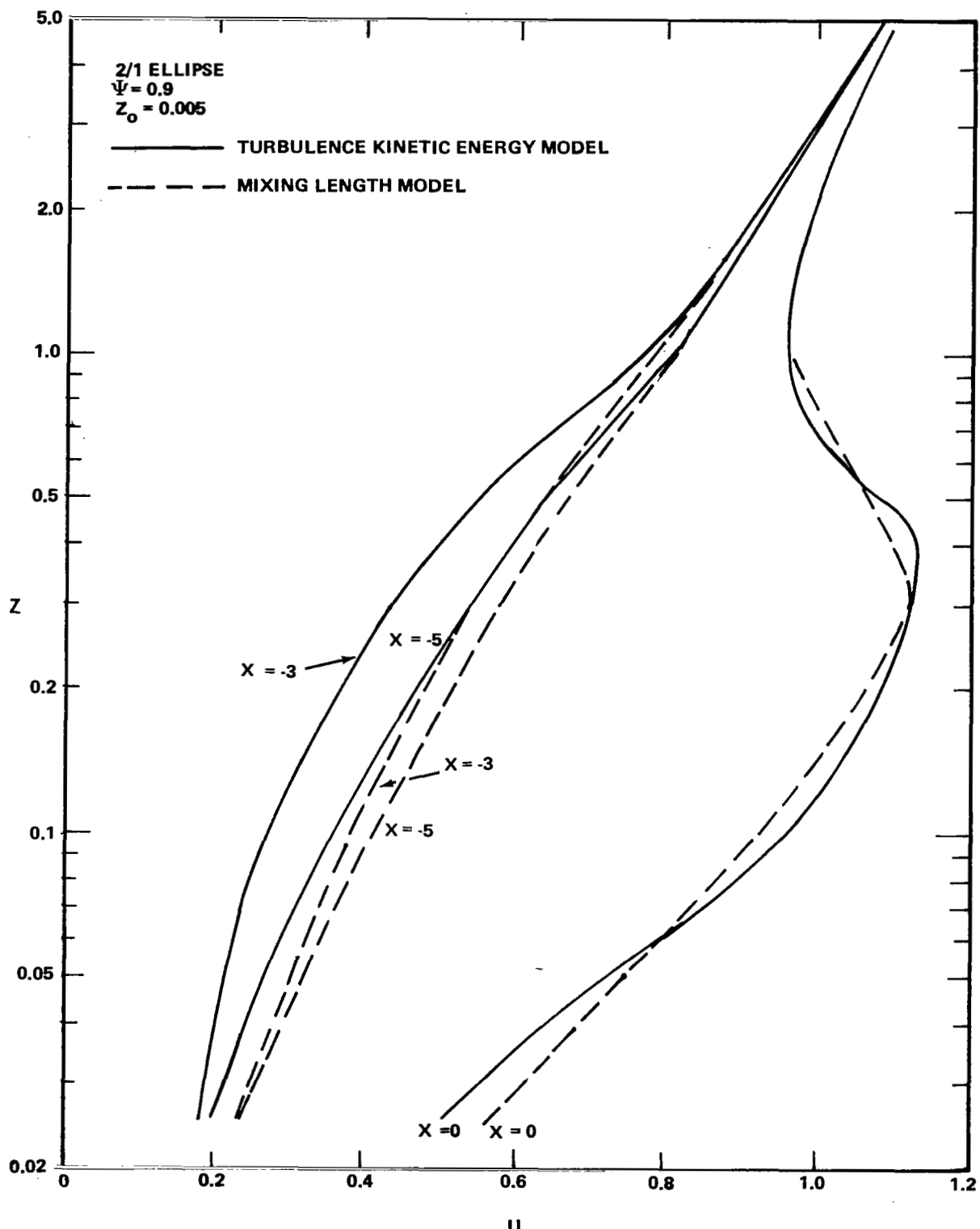
Figure 2.   Velocity Distribution Over a 2/1 Ellipse for
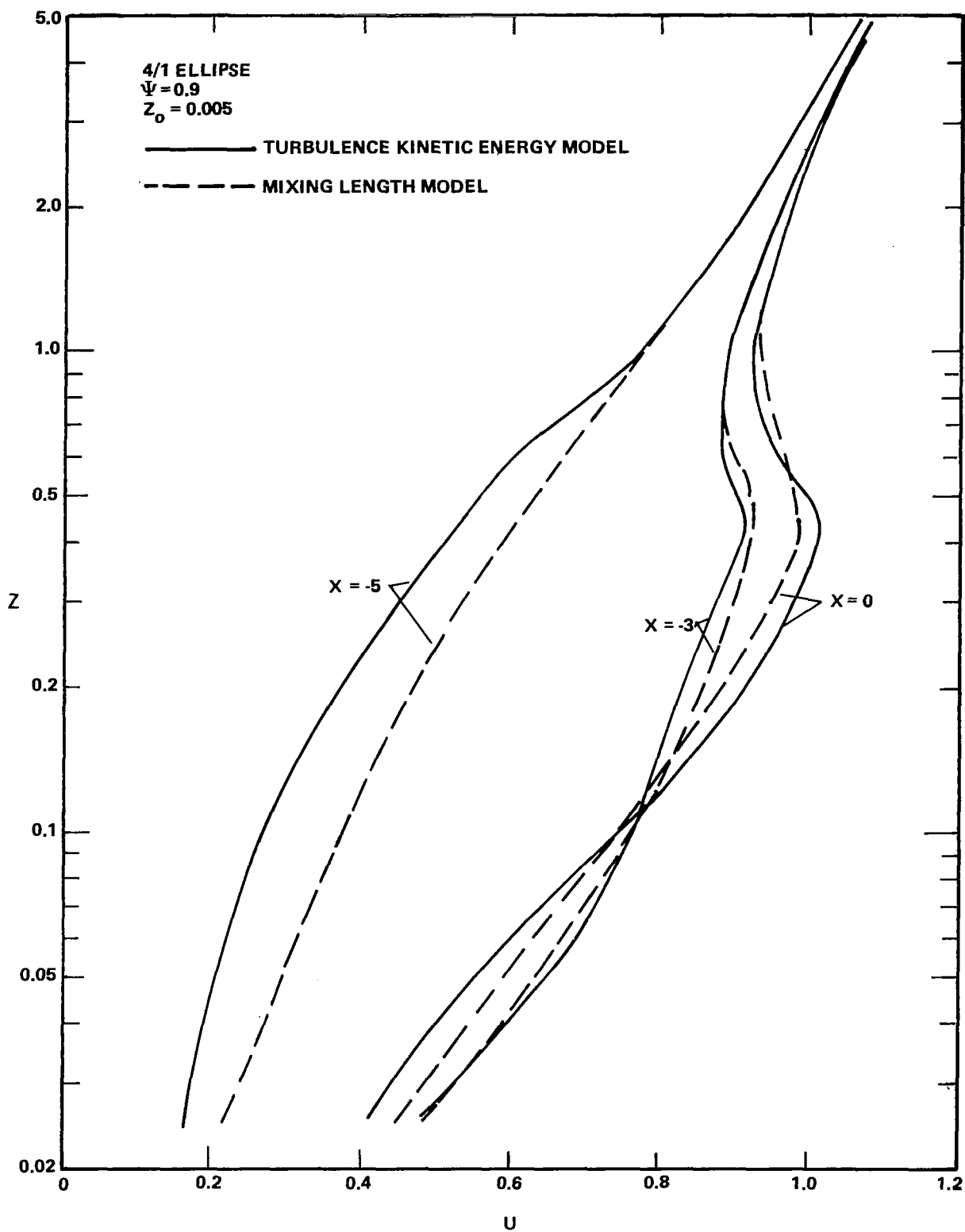Turbulence Kinetic Energy and Mixing Length
Models.

29

Figure 3. Velocity Distribution Over a 4/1 Ellipse for
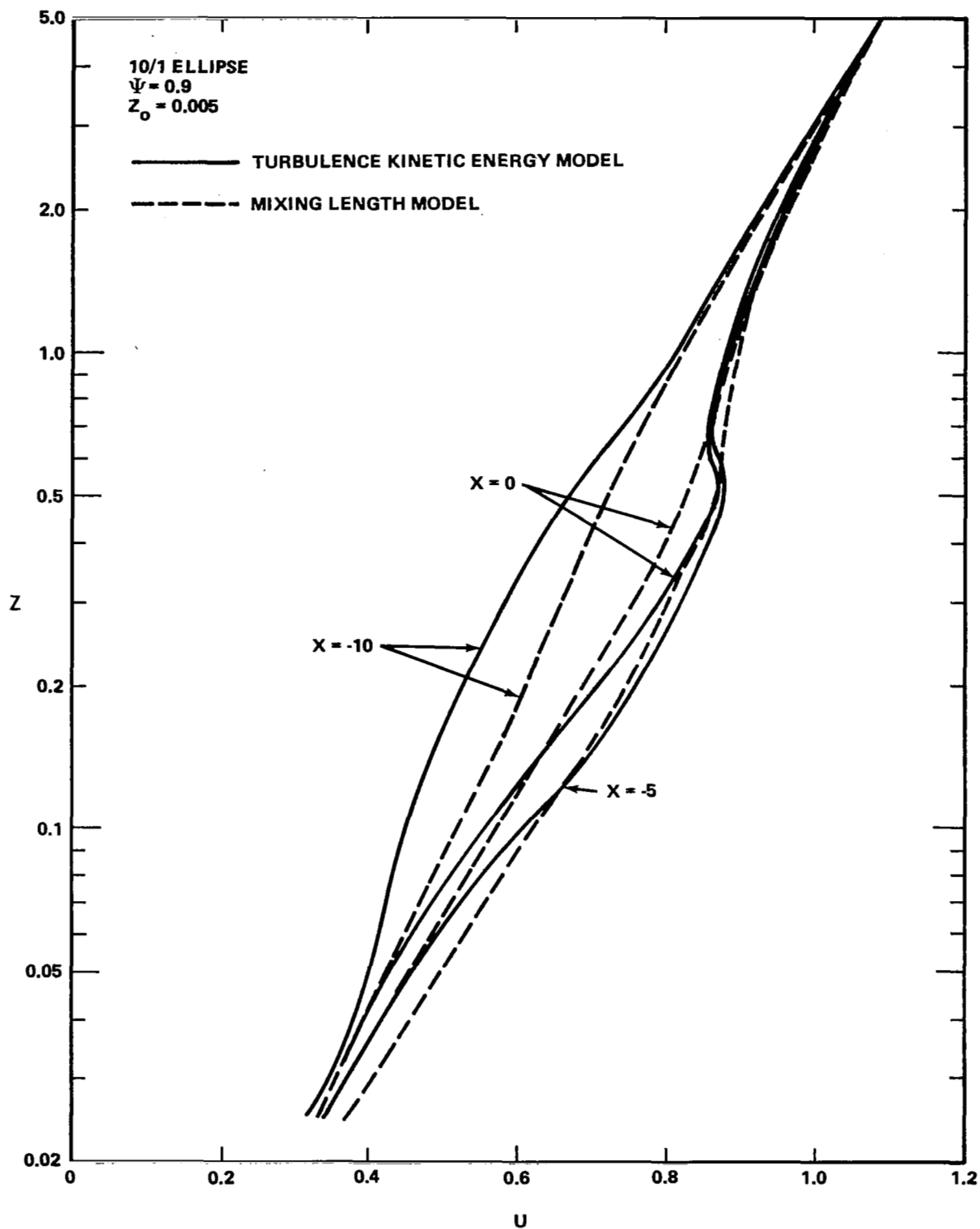Turbulence Kinetic Energy and Mixing Length
Models.

Figure 4. Velocity Distribution Over a 10/1 Ellipse for Turbulence Kinetic Energy and Mixing Length Models.

31

where

$$\ell^* = \kappa(z^* + z_o^*)$$

which is the Prandtl mixing length hypothesis.

The production, diffusion, dissipation, and convection terms are plotted versus x in Figures 5, 6, and 7 at elevations of z equal to 0.063, 0.206, and 0.42 respectively. Also, plotted in each figure are the velocities at the given z for the TKE model and the PML model.

For all three values of z, the production term is larger than the dissipation term in the major part of the adverse pressure gradient region x < -5. This reflects an imbalance between production and dissipation in the adverse pressure gradient region with the TKE model which would not occur with the PML model, since the production and dissipation are equal in the latter model. The production term is a measure of the rate at which kinetic energy is extracted from the mean flow and converted into turbulence kinetic energy. Therefore, more kinetic energy is removed from the mean flow in the adverse pressure gradient region for the TKE model than for the PML model, resulting in a greater deceleration of the flow.

In the favorable pressure gradient region, x > -5, the behavior of the models varies with respect to each other depending on the height z. Near the surface (z ≃ 0.063), Figure 5, the production term of the TKE model is less than the dissipation term in the initial portion of the favorable
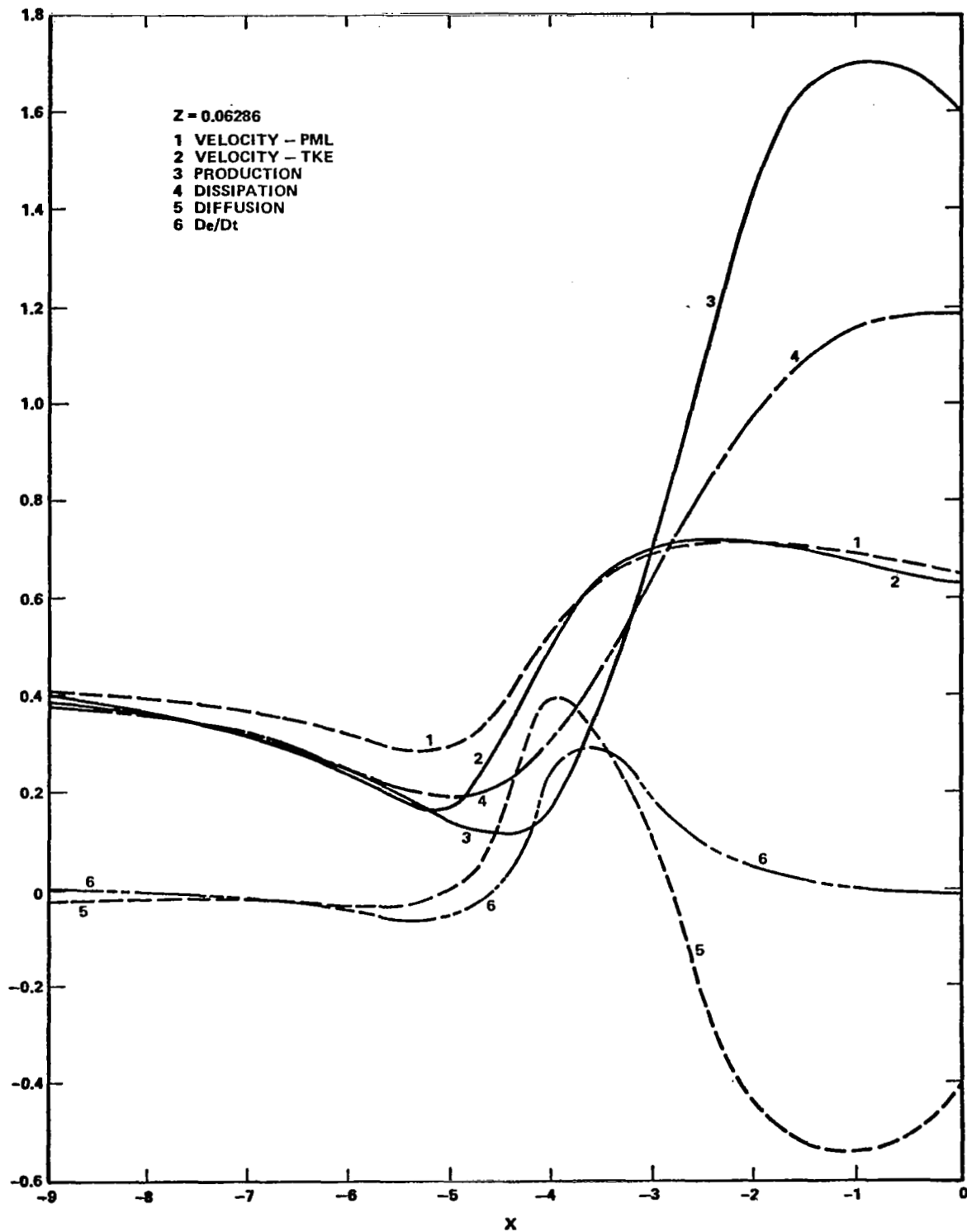
32

Figure 5. Turbulence Kinetic Energy Production Dissipation, Diffusion, and Convection Versus Distance Upstream from Top of Ellipse at z = 0.063.
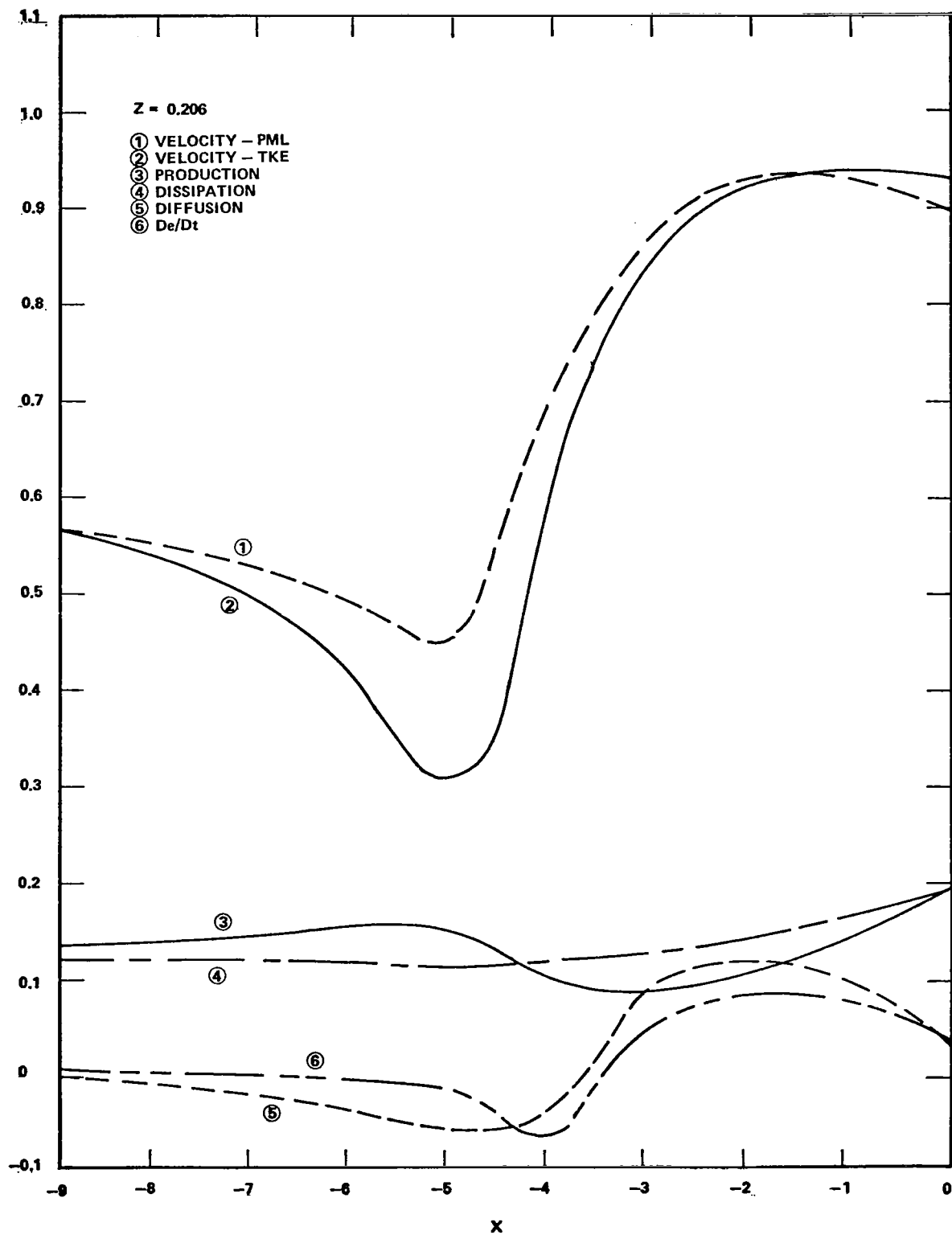
33

Figure 6.   Turbulence Kinetic Energy Production, Dissipation,
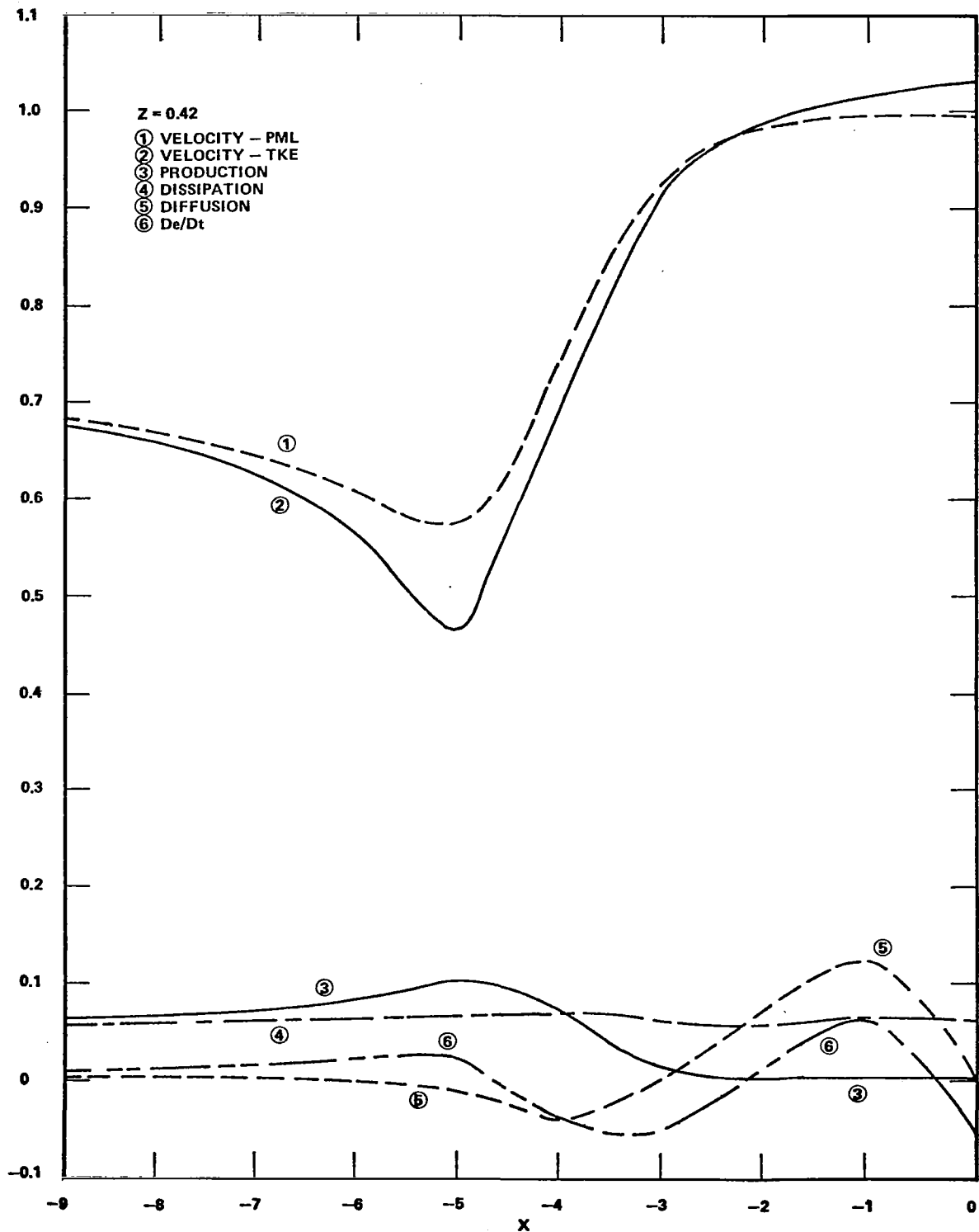Diffusion, and Convection Versus Distance Upstream
from Top of Ellipse at z = 0.206.

34

Figure 7.   Turbulence Kinetic Energy Production, Dissipation,
Diffusion, and Convection Versus Distance Upstream
from Top of Ellipse at z = 0.42.

35

pressure gradient region (-5 < x < -3), implying that less kinetic energy is removed from the mean flow by the TKE model than by the PML model. This results in greater acceleration of the flow by the pressure gradient so that the velocity for the TKE model catches up to and overshoots that of the PML model.

In the portion of the region of favorable pressure gradient from x > -3 to x = 0, production again exceeds dissipation for the TKE model. More kinetic energy is extracted from the mean flow so that the flow predicted by the TKE model now accelerates at a lesser rate, allowing the velocity for the PML model to overtake the TKE model velocity.

Further from the surface at z = 0.206 and 0.42, Figures 6 and 7, production is less than dissipation for the TKE model, resulting in greater acceleration by the pressure gradient so that the velocities for TKE model overshoot those for the PML model at the top of the ellipse.

The differences in behavior of the production and dissipation terms at different heights above the surface can possibly be explained by wall effects on the flow very near the surface.

In the region of adverse pressure gradient, the combination of friction and pressure gradient near the surface decelerate the flow there at a greater rate than further from the surface where frictional effects are not as large and the momentum of the flow attempts to hold the velocity

constant. This tends to form a region of higher shear analogous to a free shear layer. Experimental evidence of this is shown in Figure 8, from [15], which shows peak $\overline{u'w'}$ values between the surface layer and the outer layer of the flow. As a result of this layer of increased shear, the production term, $(\tau/\rho) \, \partial u/\partial z$, tends to decrease near the surface and increase further away as the stagnation point is approached.

In the favorable pressure gradient region, the pressure gradient works against the wall friction which causes the layer of maximum shear to move toward the surface with the velocity profile becoming flatter further away. Thus the production of turbulence kinetic energy increases near the surface and decreases at higher elevations.
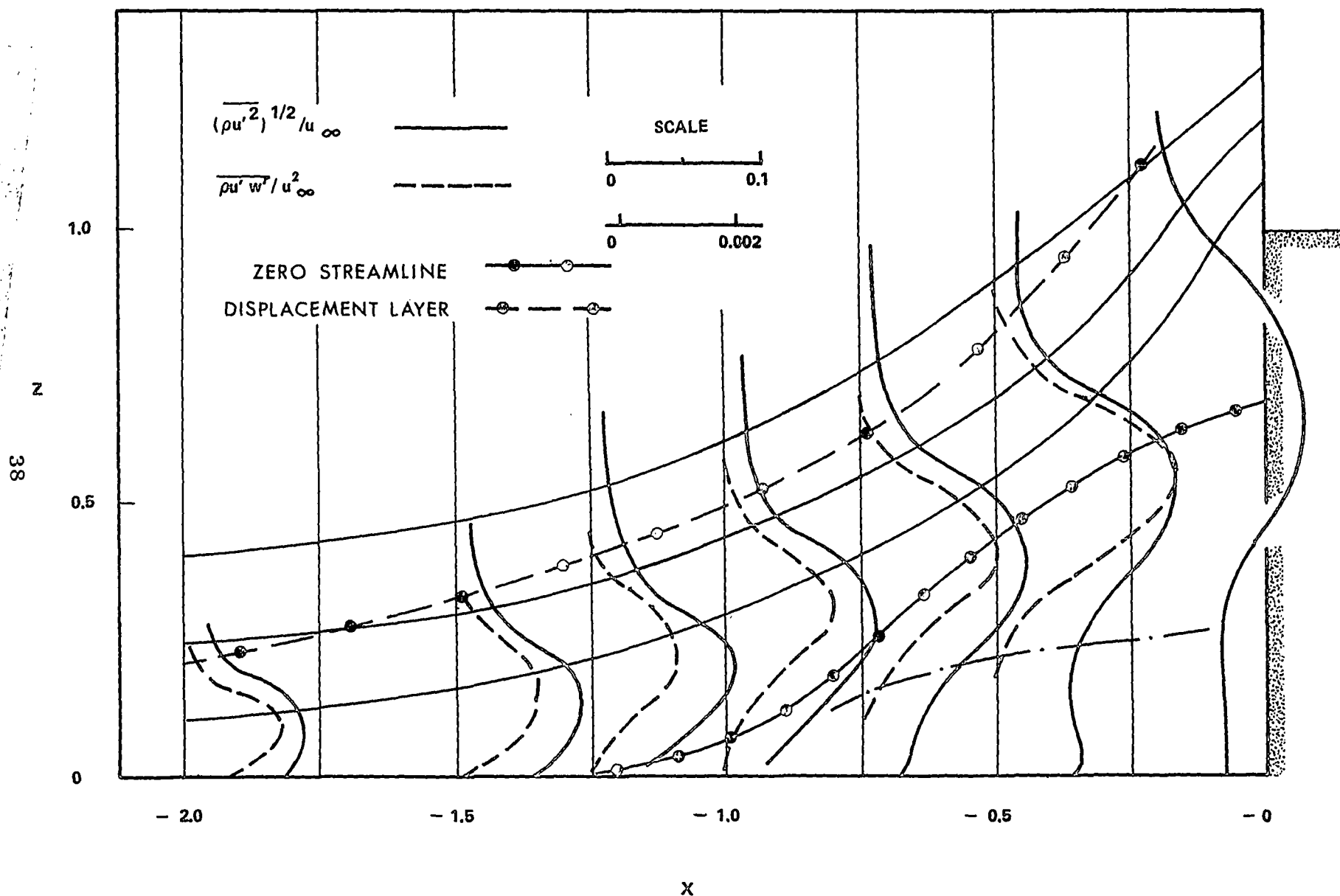
Figure 8. Turbulence Intensities and Shear Stress Profiles
b = 2.0, b/δ_r = 5.0, Re_l = 5.05 x 10^5. [15]

CHAPTER VI'

EFFECTS OF ASPECT RATIO

The effects of a variation of elliptical aspect ratio on the velocity profiles at the top of the ellipse are shown in Figures 9 and 10 for the turbulence kinetic energy model and Prandtl mixing length model respectively. For both models the effect of increasing the aspect ratio results in a decreased overshoot in velocity at the top of the ellipse.

This effect can be explained by the variation with aspect ratio of the pressure gradient distribution along the x-axis as shown in Figure 11. The regions of adverse pressure gradient are very similar for the three bodies. Therefore, the retardation of the flow in the adverse pressure gradient regions will be essentially the same. The regions of favorable pressure gradient, however, are quite different for the three bodies. The magnitude of the favorable pressure gradient increases with decreasing aspect ratio. For the 2/1 ellipse, the pressure gradient varies markedly over the entire surface of the ellipse whereas for the 10/1 ellipse the variation is only over a small region of the upstream surface. The flow is therefore much more strongly accelerated by the favorable pressure gradient of the lower aspect ratio ellipse and as a result, attains higher velocities at the top.
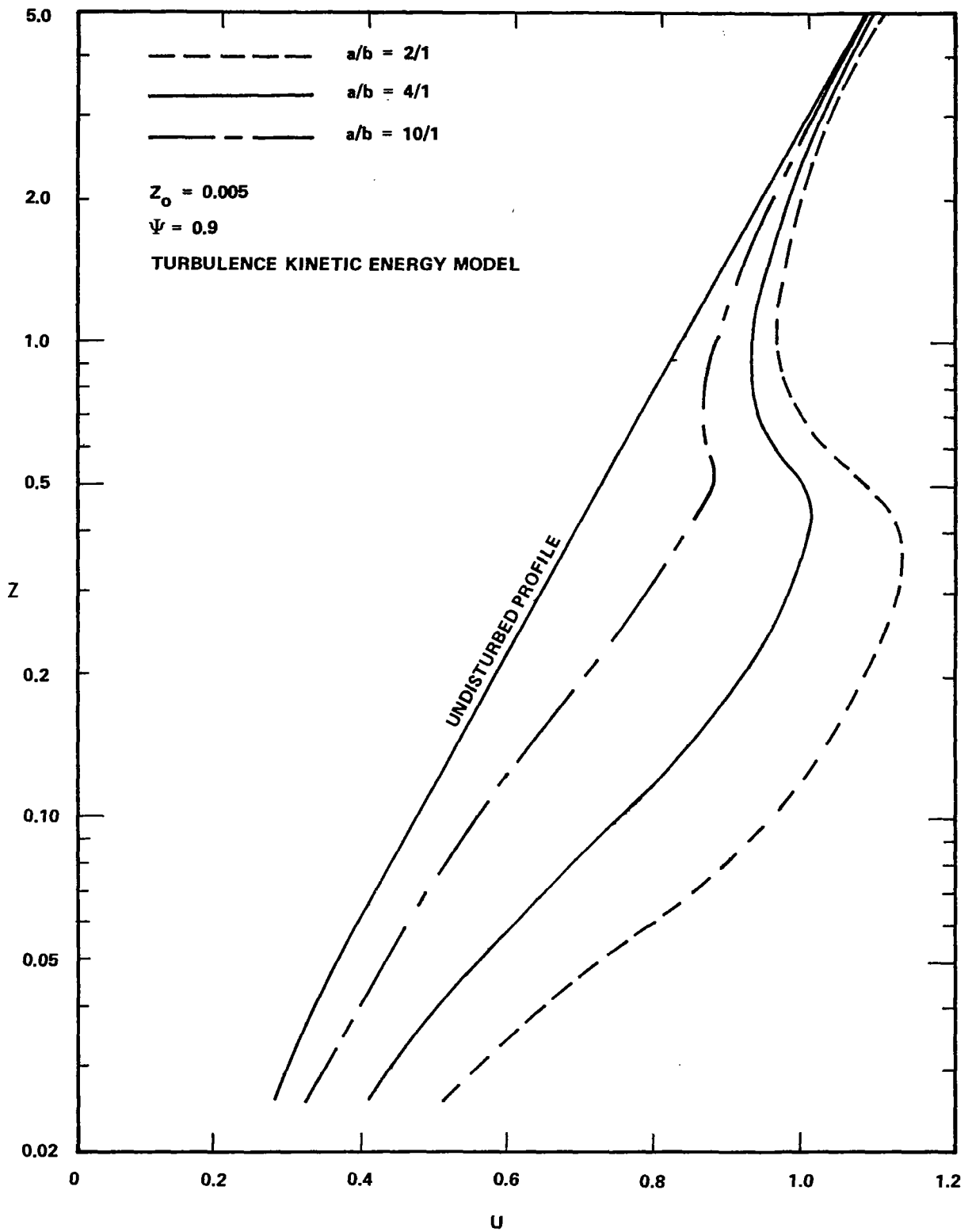
Figure 9.   Velocity Profiles at the Top of the Ellipse for
Turbulence Kinetic Energy Model for Aspect
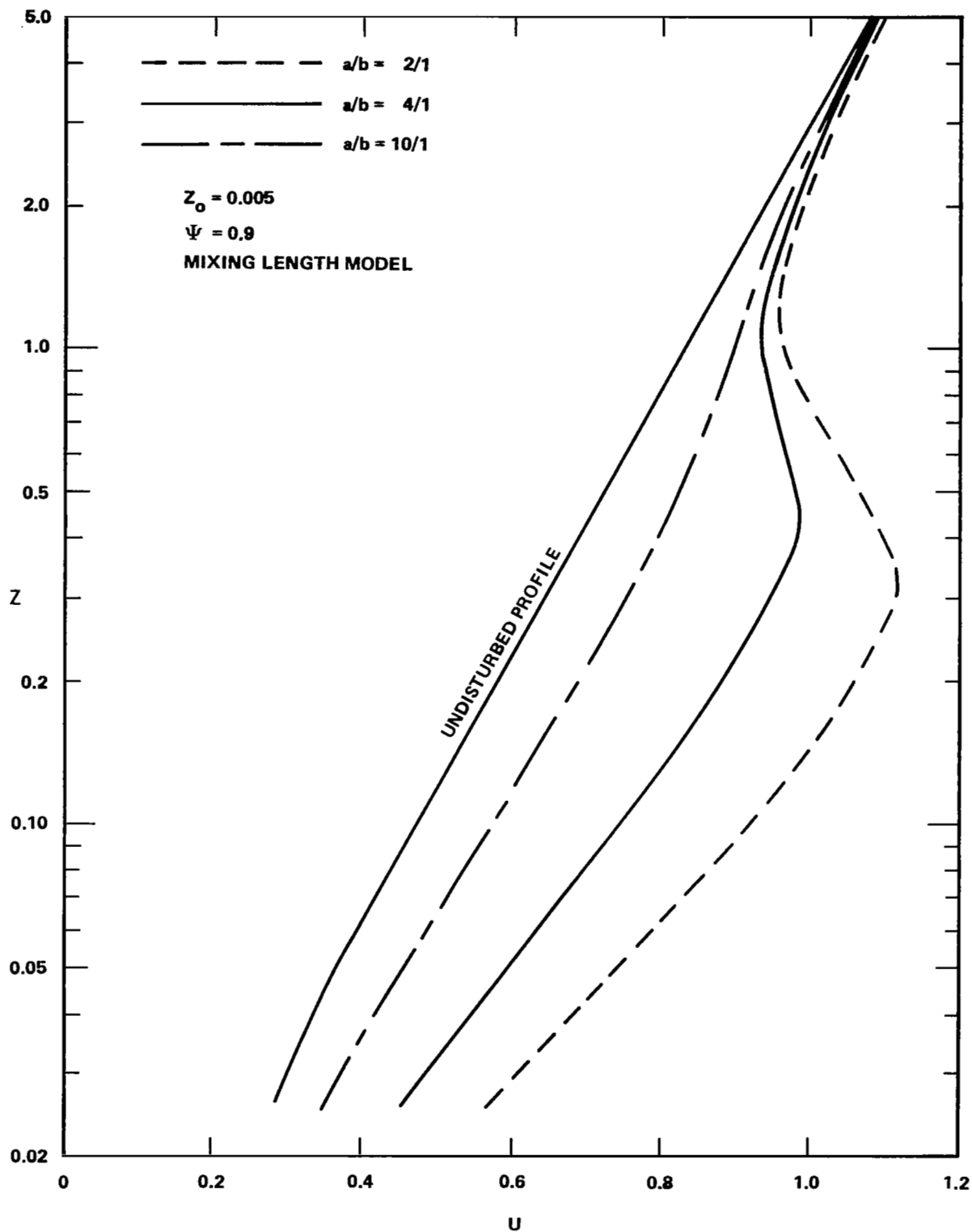Ratios of 2/1, 4/1, 10/1.

Figure 10. Velocity Profiles at the Top of the Ellipse for Prandtl Mixing Length Model for Aspect Ratios of 2/1, 4/1, 10/1.
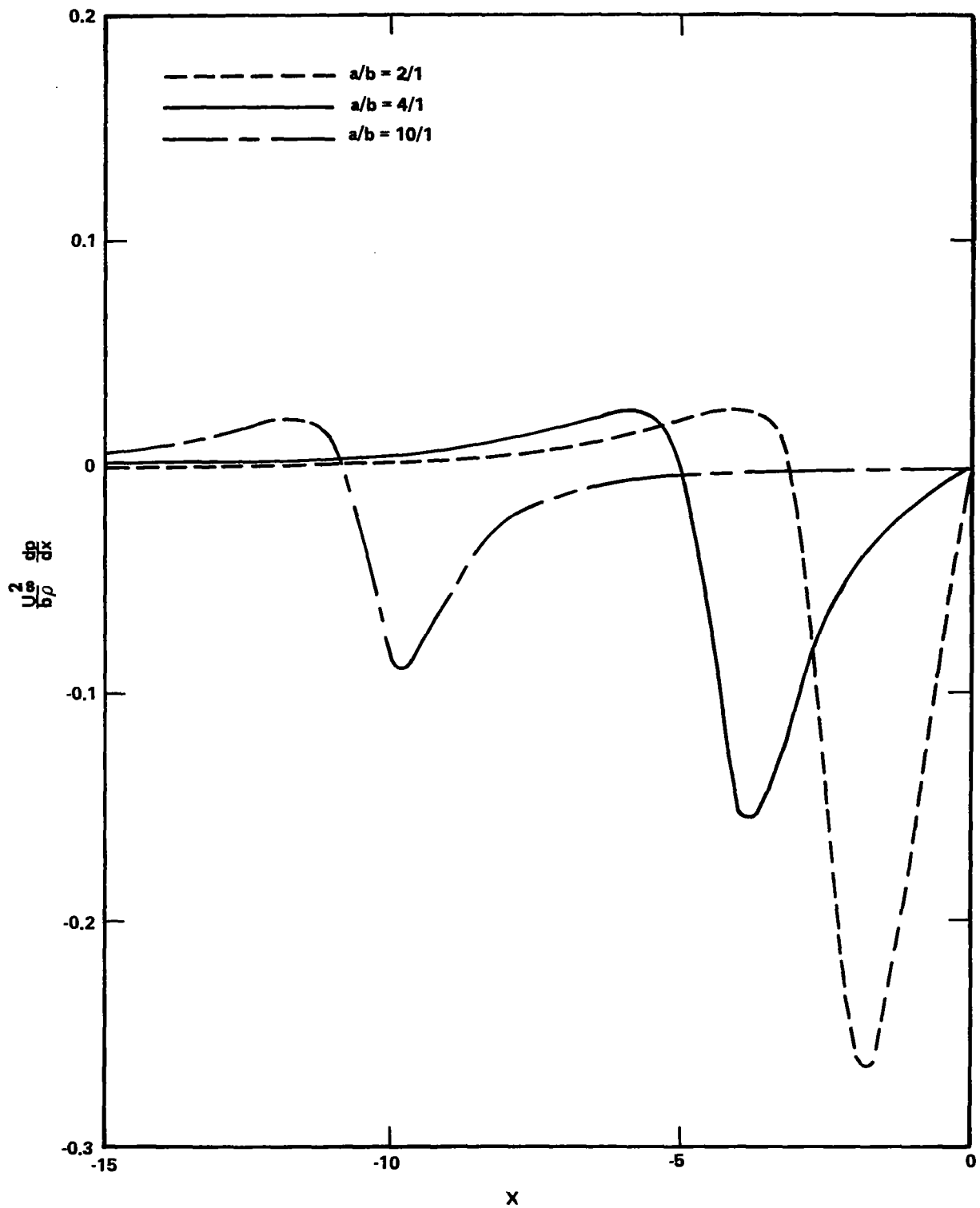
41

Figure 11. Variation of Pressure Gradient Distribution Along x-Axis with Respect to Aspect Ratio of Ellipse.

42

CHAPTER VII

INFLUENCE OF SURFACE ROUGHNESS AND ASPECT
RATIO ON SEPARATION

The adverse pressure gradients upstream of the body cause separation of the boundary layer near the stagnation region. The point at which this separation occurs can be determined by solving the governing equations discussed previously, using the pressure distribution given by the potential flow solution for the streamline $\psi = 0$. This was done for a number of surface roughnesses and aspect ratios. The results of the calculations are shown in Figure 12.

The length of the forward separation bubble, λ, decreases with decreasing surface roughness and/or increasing aspect ratio. This behavior of the separation bubble is similar to that for the Prandtl mixing length model [4], except that separation occurs further upstream for the TKE model in all cases. This is to be expected because of the greater retardation of the flow in the adverse pressure gradient region described previously for the TKE model.
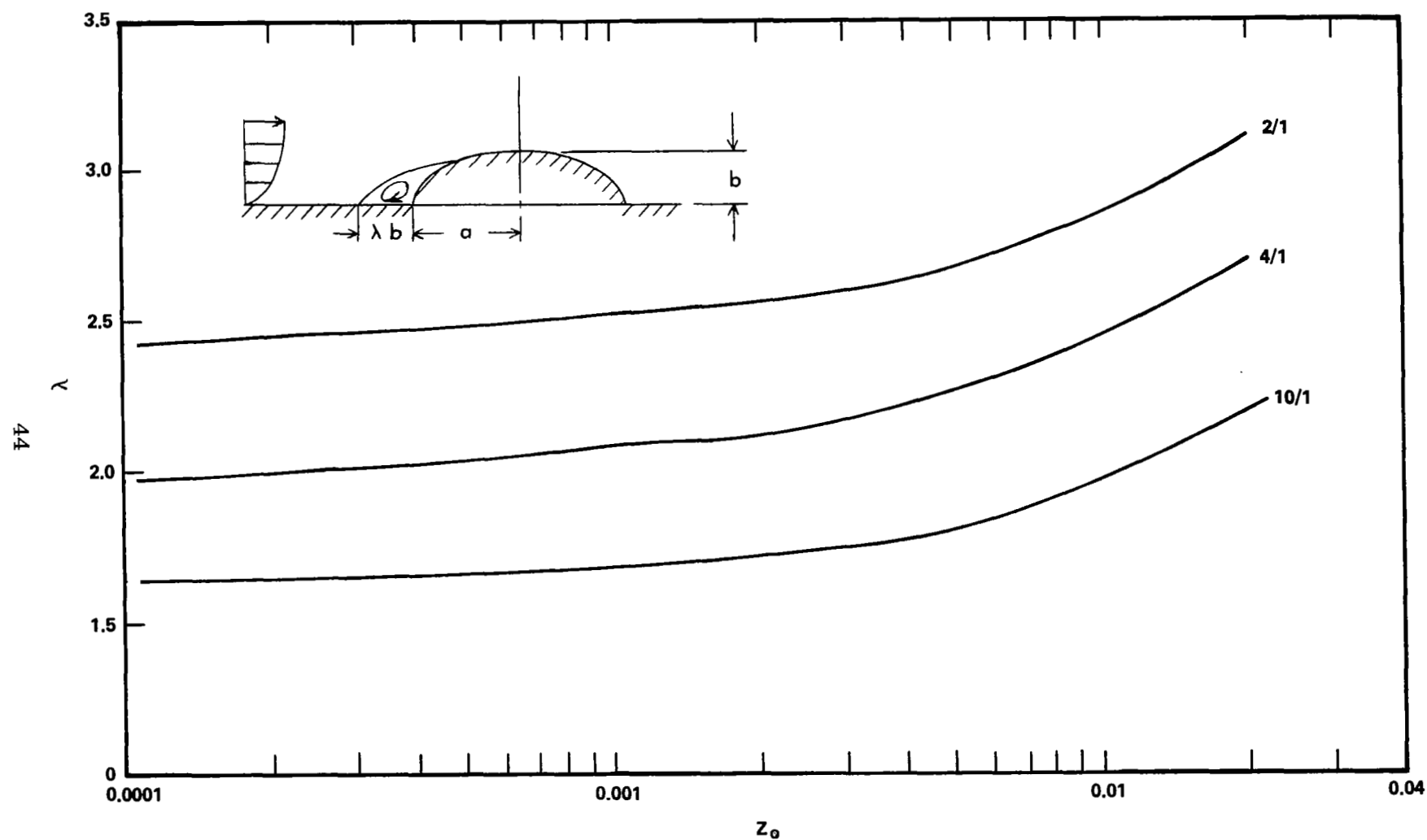
Figure 12. Effects of Surface Roughness and Aspect Ratio on Length
of Separation Bubble, λ.

CHAPTER VIII

TURBULENCE INTENSITY DISTRIBUTION NEAR
AN ELLIPTICAL OBSTRUCTION

If an aircraft is to fly over an obstruction in the wind field at low altitude, it is necessary to be able to predict regions of high turbulence levels so that the pilot can avoid these areas or at least be prepared to encounter the turbulence.

The distribution of turbulence intensity,

$$\hat{u}' \equiv \sqrt{1/3\,(\overline{u'^2} + \overline{v'^2} + \overline{w'^2})}/U_\infty \qquad (34)$$

over an elliptical body with an aspect ratio of 4/1 is shown in Figure 13. The turbulence intensity is greatest near the body and is nearly uniform above an altitude of twice the height of the ellipse. There is a local maximum in turbulence intensity above the stagnation point.

The turbulence intensity distribution is proportional to the square root of the turbulence kinetic energy distribution, since, from Equations (2) and (34)

$$\hat{u}' = \sqrt{2/3\,e}/U_\infty \qquad (35)$$

The turbulence kinetic energy distribution is shown in Figure 14. The variations of the turbulence kinetic energy in the flow field is related to the behavior of the convection term of the turbulence kinetic energy equation (Figure 15). The convection term indicates the rate of convection
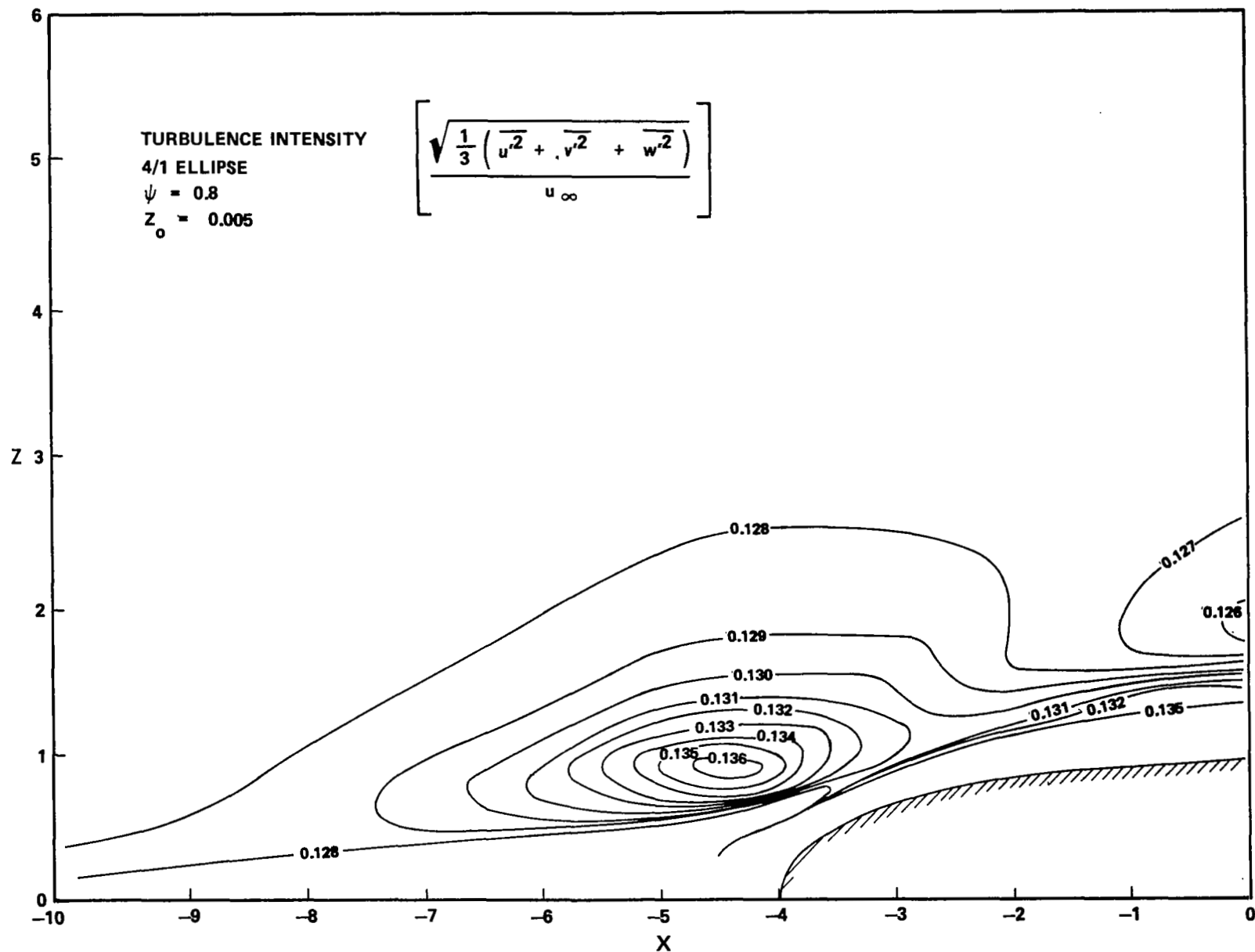
45

Figure 13. Distribution of Turbulence Intensity Over
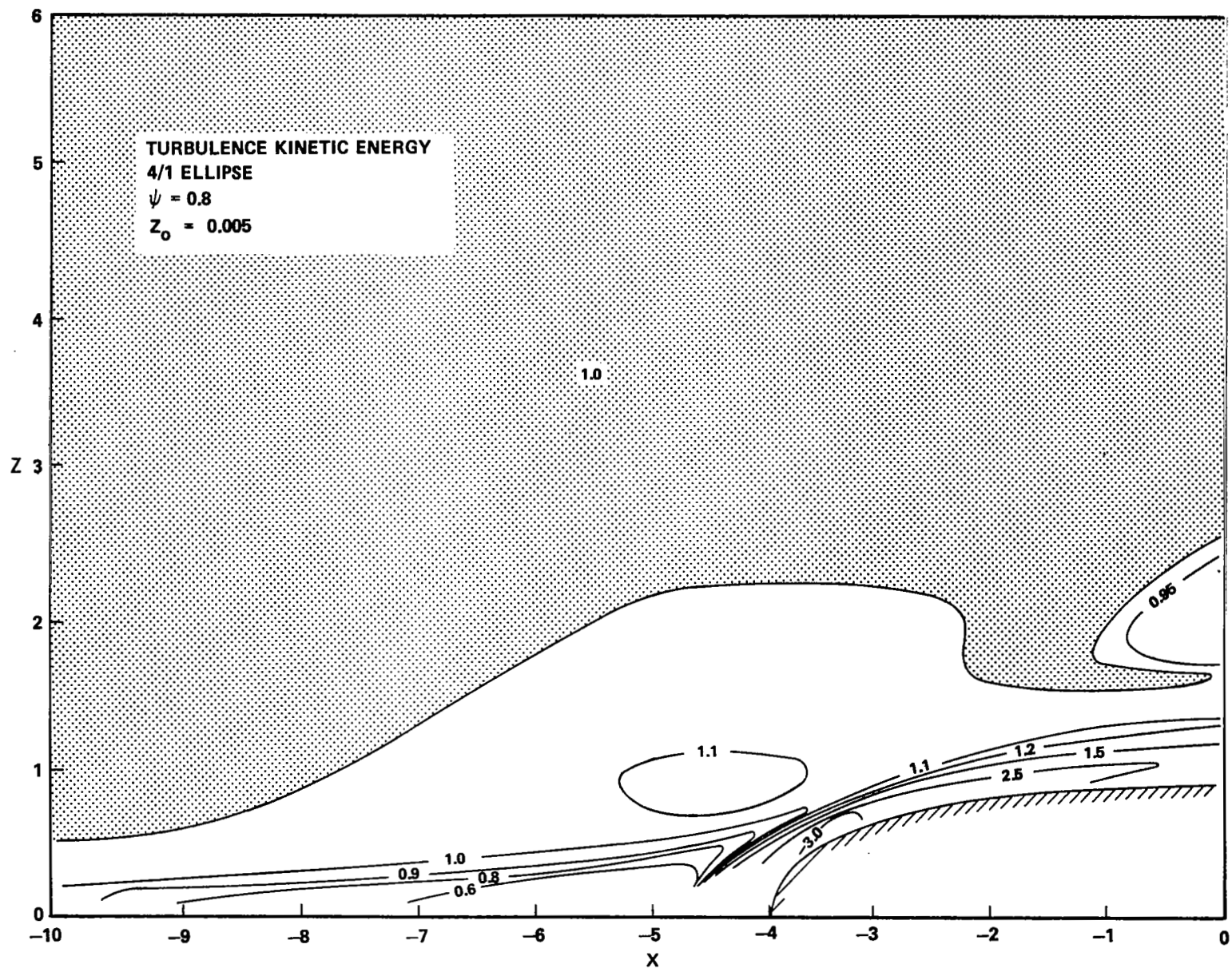4/1 Ellipse.

Figure 14.   Distribution of Turbulence Kinetic Energy
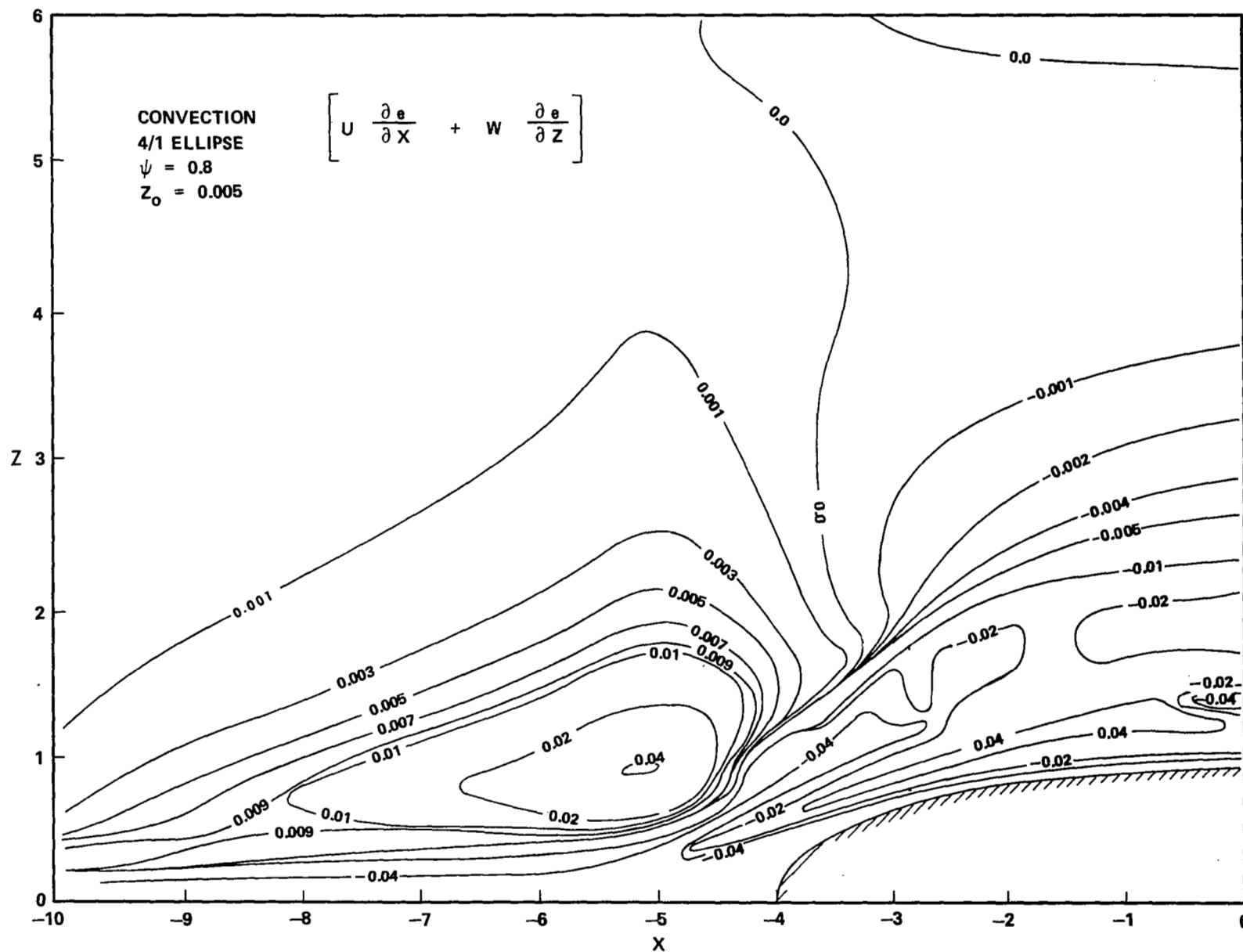Over 4/1 Ellipse.

Figure 15. Distribution of Turbulence Kinetic Energy Convection Over
4/1 Ellipse.

of turbulence kinetic energy toward or away from a given point. A positive value of the convection term in a given area indicates convection away from the area, while a negative value indicates convection toward the area. The areas where the turbulence kinetic energy is increasing in the downstream direction correspond to areas where the convection term is positive, and areas of decreasing turbulence kinetic energy correspond to a negative convection term.

The convection term is the sum of the production and diffusion terms (Figures 16 and 17 respectively) minus the dissipation term (Figure 18). The sign of the convection term is primarily determined by the production and dissipation terms, which are an order of magnitude greater than the diffusion term in most areas. A positive convection term indicates that production is greater than dissipation, requiring convection of turbulence kinetic energy to surrounding areas, the reverse being true in areas of negative convection.

The peak in turbulence kinetic energy near the stagnation point occurs where the flow near the surface is retarded by the friction at the wall, while the flow at a greater distance from the wall is accelerated by a favorable pressure gradient, which decreases with increasing height to match the free stream logarithmic velocity profile. The steep turbulence kinetic energy (and turbulence intensity) gradients occurring near the wall in this area are due to the transition from an adverse to a favorable pressure
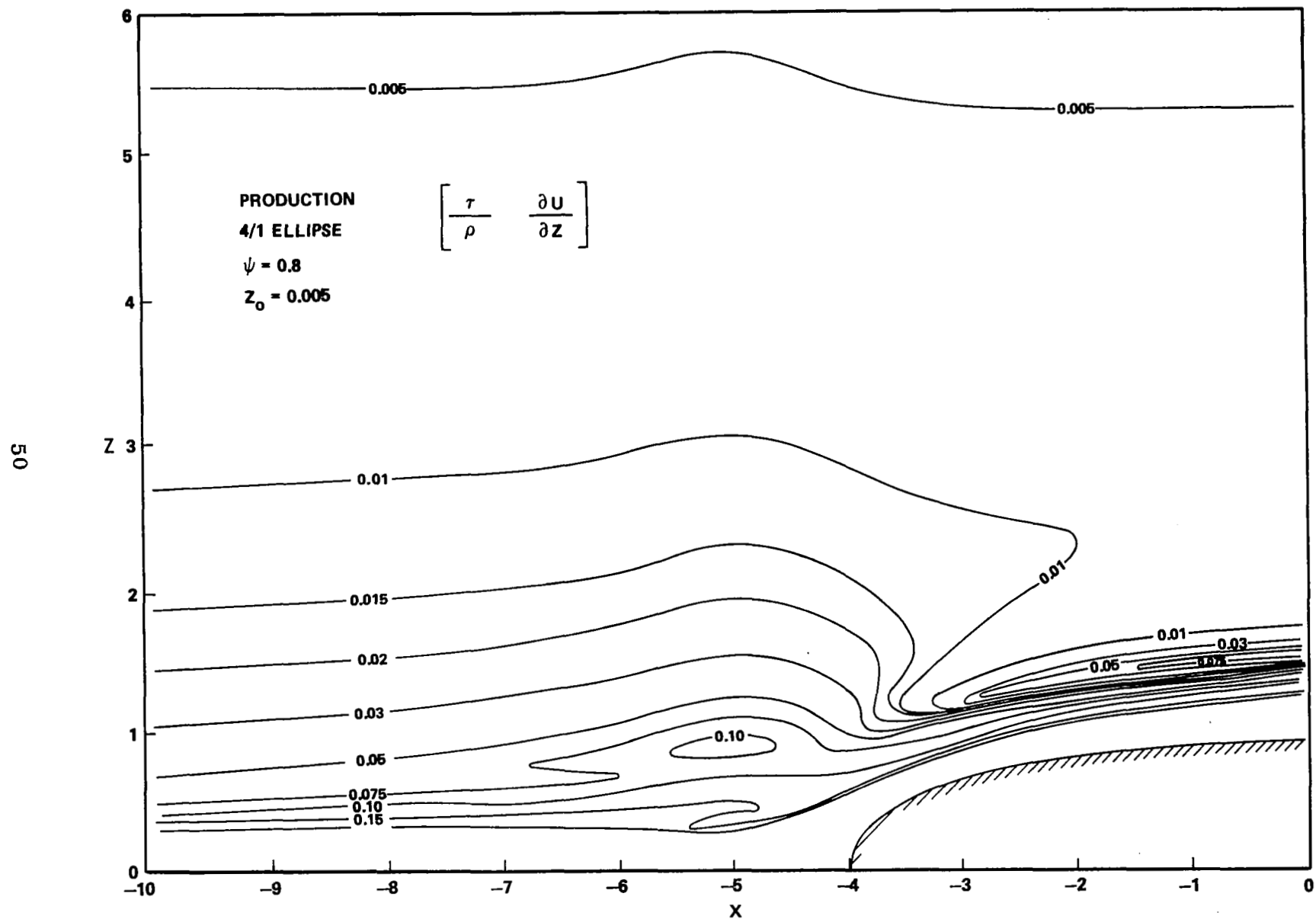
Figure 16.   Distribution of Turbulence Kinetic Energy Production Over 4/1 Ellipse.
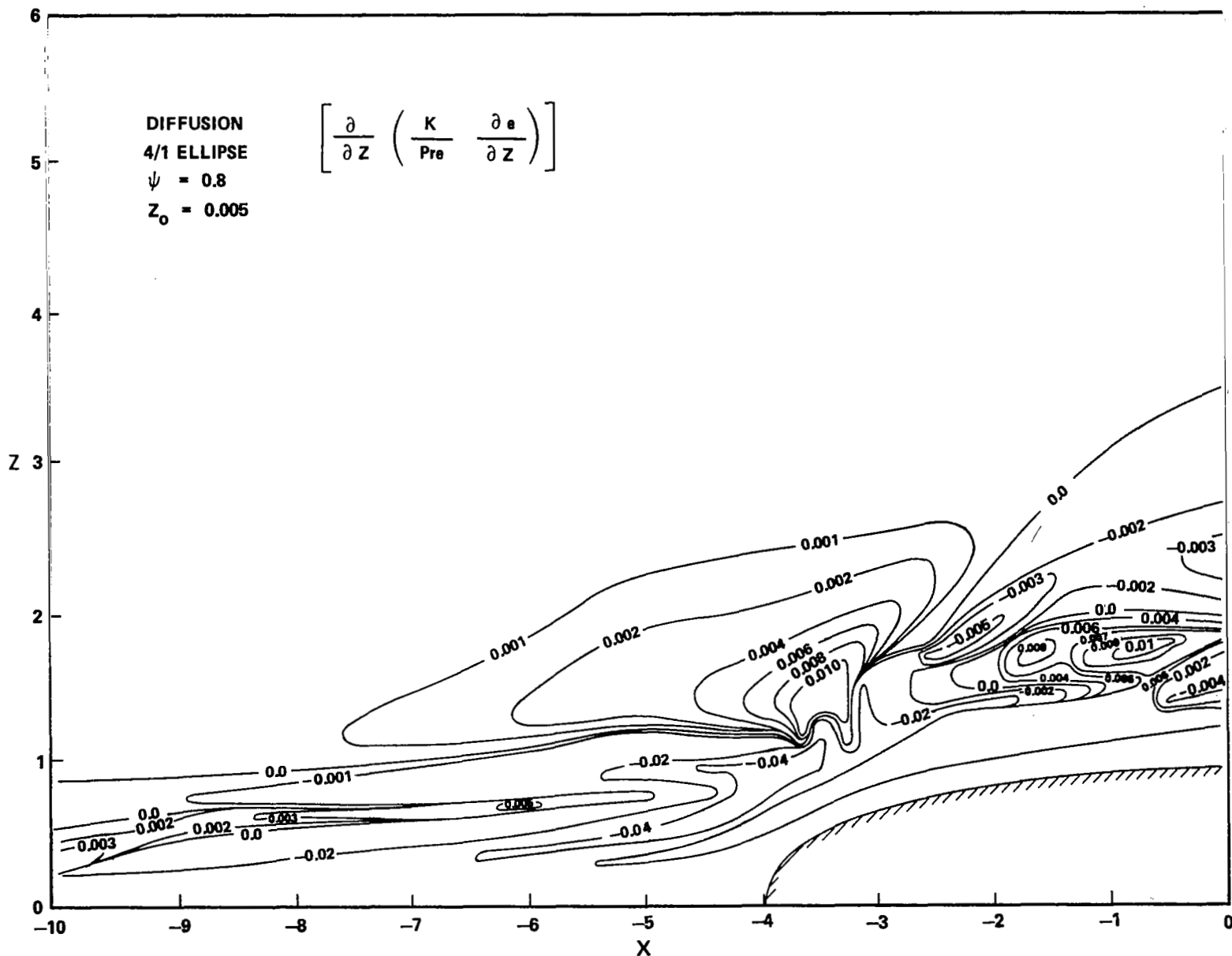
50

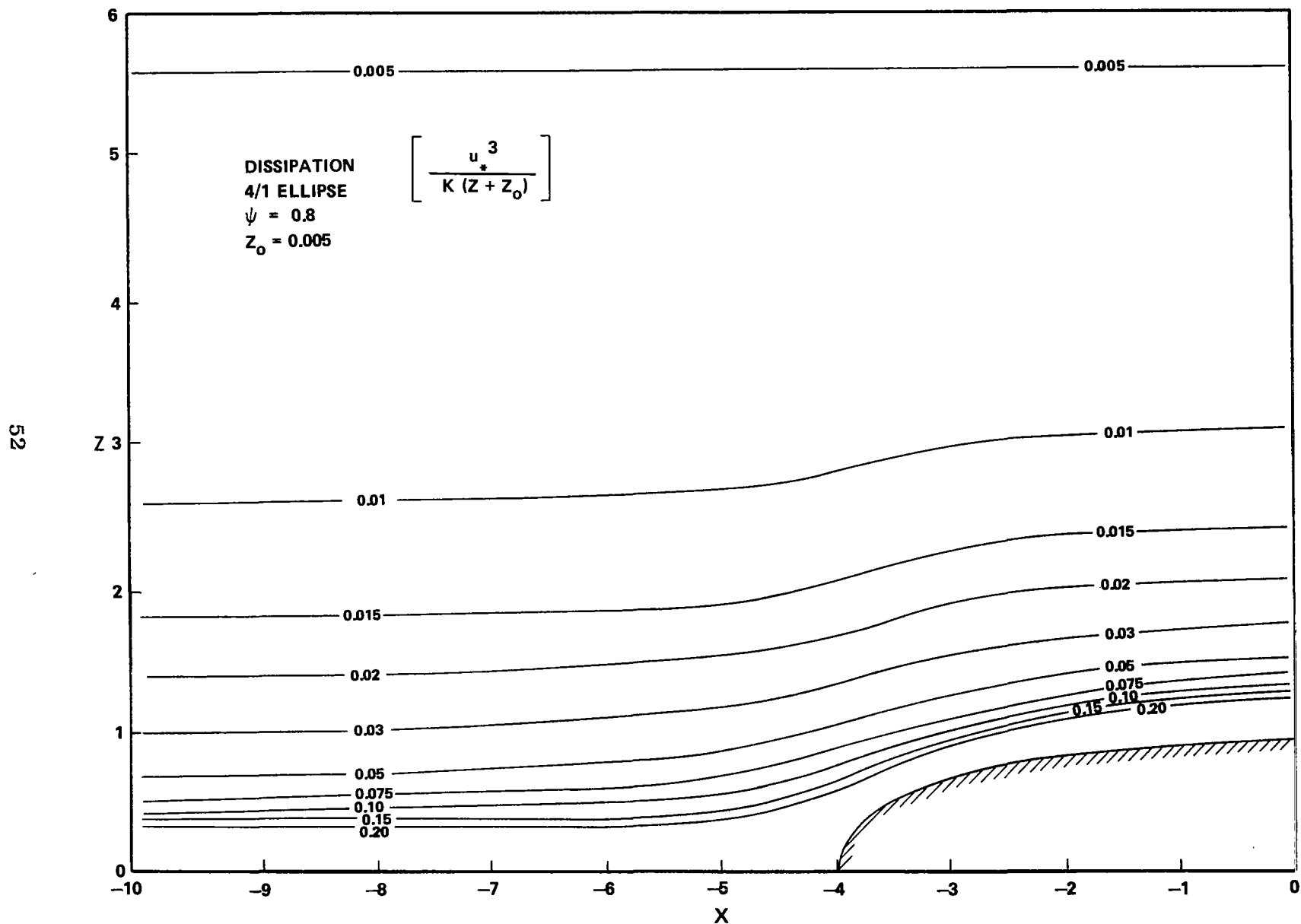Figure 17.   Distribution of Turbulence Kinetic Energy Diffusion Over 4/1 Ellipse.

Figure 18.   Distribution of Turbulence Kinetic Energy Dissipation Over

gradient.

The slight local minimum in turbulence kinetic energy between $x \simeq -1$ and $x = 0$ at $z \simeq 2$ is due to the velocity decreasing from its peak value at $z \simeq 1.5$ in order to match the free stream logarithmic profile (Figure 3, page 30). This results in a region of low shear stress near $z = 2$.

An aircraft flying over this elliptical body at an altitude less than twice the ellipse height would experience increased turbulence with decreased wind velocity at $x \simeq -4$, and increased turbulence and wind velocity over the top of the ellipse. The intense turbulence zones may prove to be unexpected hazards during landing over elliptical surface obstructions.

CHAPTER IX

DISCUSSION OF RESULTS RELATIVE TO

AERONAUTICAL APPLICATIONS

An assessment of the influence of the wind disturbance
created by a semi-elliptical terrain irregularity on air-
craft operations through the disturbance is given in this
section. The wind environment encountered along the flight
paths for CTOL and STOL aircraft relative to the FAA surface
obstruction clearance recommendations is discussed in rela-
tion to experiments and analytical studies reported in the
literature on aircraft airworthiness as influenced by wind.

Turbulence

If one considers the elliptical surface to be a hill
over which approaches are made, the flight paths for CTOL
and STOL aircraft based on FAA surface obstruction clearance
standards (see [16, 17]) would be as shown in Figure 19. In
general the aircraft passes through only the fringes of the
disturbance with the STOL aircraft experiencing at most a
region of turbulence kinetic energy approximately 10 percent
higher than the undisturbed atmospheric value. Assuming a
9 m/sec wind in the undisturbed flow at a height of three
times that of the hill, gives σ_u = 1.41 m/s in the undis-
turbed region and σ_u = 1.48 m/s in the portion of the dis-
turbed region through which the airplane passes.

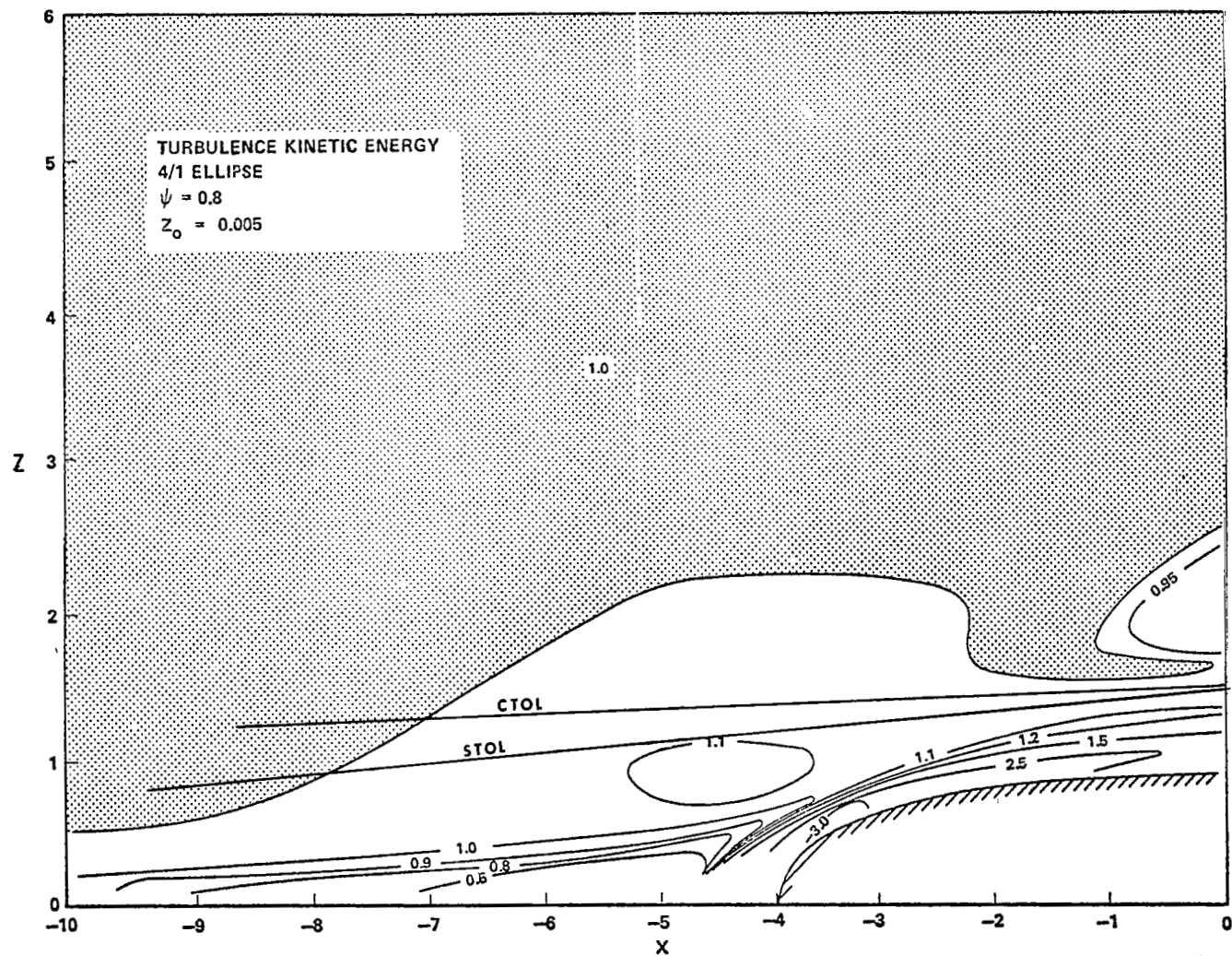Neuman and Foster [18] have observed that with

54

Figure 19. Typical Flight Paths Through the Turbulent Region **Above** a Semi-Elliptically Shaped Obstruction.

σ_u = 1.83 the tentative FAA spec.fication of 0.9 m/s maximum rate of descent is exceeded 45 pe. cent of the time. Assuming two Gaussian distribution; with standard deviations of 1.41 m/s and 1.48 m/s, respectively, the probability of exceeding 1.83 m/s for each distribution can be predicted. The probability of a hard landing is then 45 percent,times the probability that 1.83 m/s will be exceeded. Based on this analysis there is a 10 percent higher chance of a hard landing than in the natural atmosphere which due to the crude nature of the analysis is seemingly negligible. Hence the FAA clearance surface requirements for STOL ports appear adequate for approaches over the windward part of curved proturbances. However, if one envisions landing on a strip on top of a plateau or hill, the aircraft will encounter considerably higher turbulence. On the top of the elliptical surface, the ratio of the rms components in the disturbed flow to that in the undisturbed flow can be as high as 1.58 given σ_u = 2.23 m/s. The probability of hard landings in this case is, according to the crude analysis, 100 percent greater than in the undisturbed atmosphere. The above conclusions are obviously overly pessimistic since the more intense turbulence considered here occurs only in patches whereas the results of Neuman and Foster [18] assume continuous homogenous turbulence.

Mean Wind

Figure 20 shows the variation in the horizontal mean wind along the flight path for STOL and CTOL aircraft over
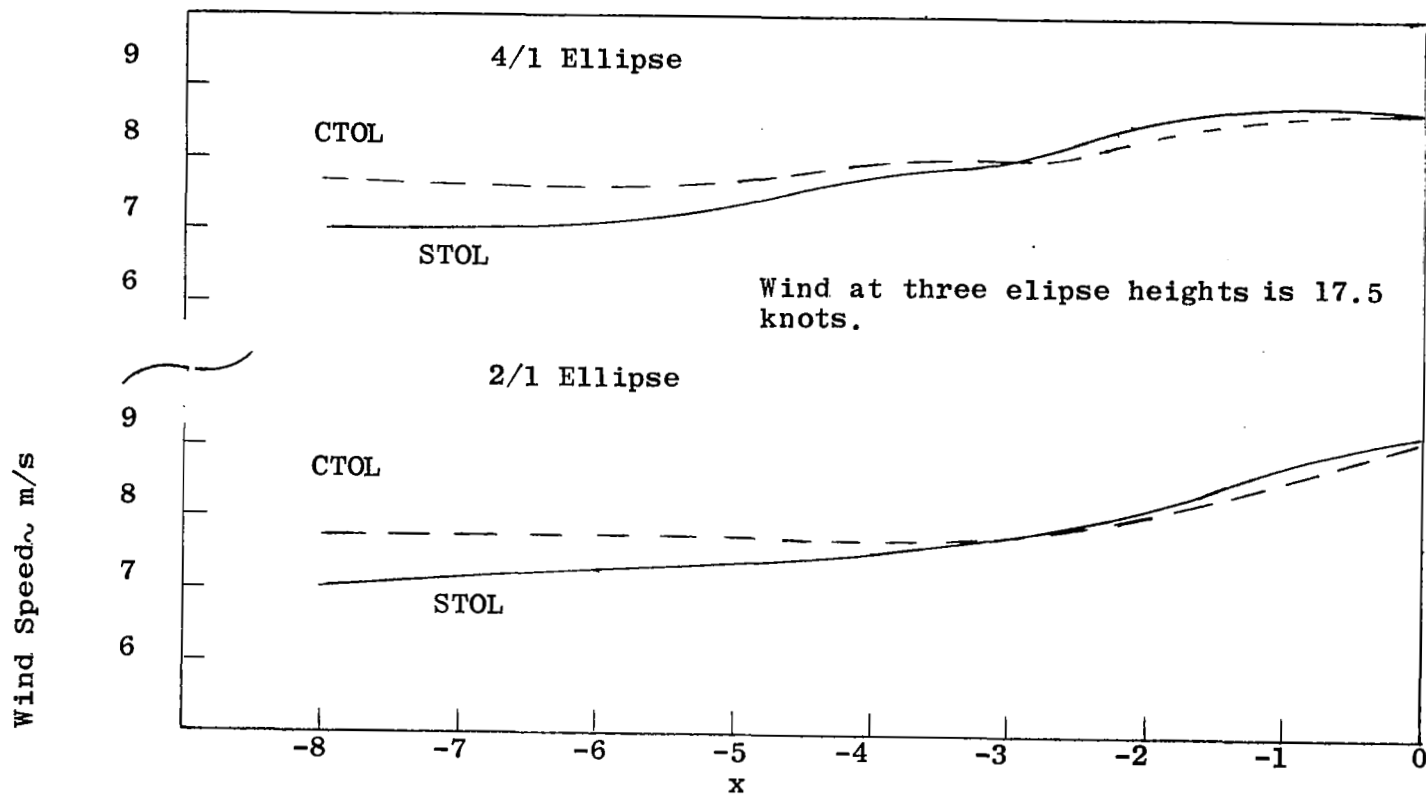
Figure 20.   Wind Speed Variation Along Typical Flight Paths

the 4/1 and 2/1 ellipse respectively. For the STOL aircraft
passing over the 2/1 ellipse there is approximately a 2/ms
change in velocity over a horizontal distance of eight semi-
ellipse heights. The CTOL aircraft "sees" less wind varia-
tion along the glide slope due to its less steep approach
path. If one considers an airplance landing at 80 kts over
a 5 m hump the 2 m/s (approximately 4 kts) velocity change
will be experienced in approximately 0.97 sec. Adding the
$\sigma_u = 1.48$ m/s value to the 2 m/s value the variation in wind
will appear to the aircraft as a gust approaching the order
of the 6 m/s lateral gust value over a 0.7 sec period
reported by McManus [1]. These gusts were observed during
experiments with automatic landing of the Trident and their
effect was that the autopilot controlled the bank during the
increase in gust but could not keep pace with the decay,
consequently the aileron drove the aircraft away from the
wings level condition. Although not disastrous, such gusts
did cause the aircraft to deviate significantly from the
desired flight path while the autopilot reestablished
integration.

In this same vein, Corbin and Goddard [19] have
examined the effect of longitudinal gusts on experimental,
automatic flight control systems for the BAC 1-11. Their
predicted maximum rate of descent at touchdown as a function
of gust strength is shown in Figure 21. Gusts of 2 m/s (4 kt)
magnitude are observed to give touchdown rates between 1.1
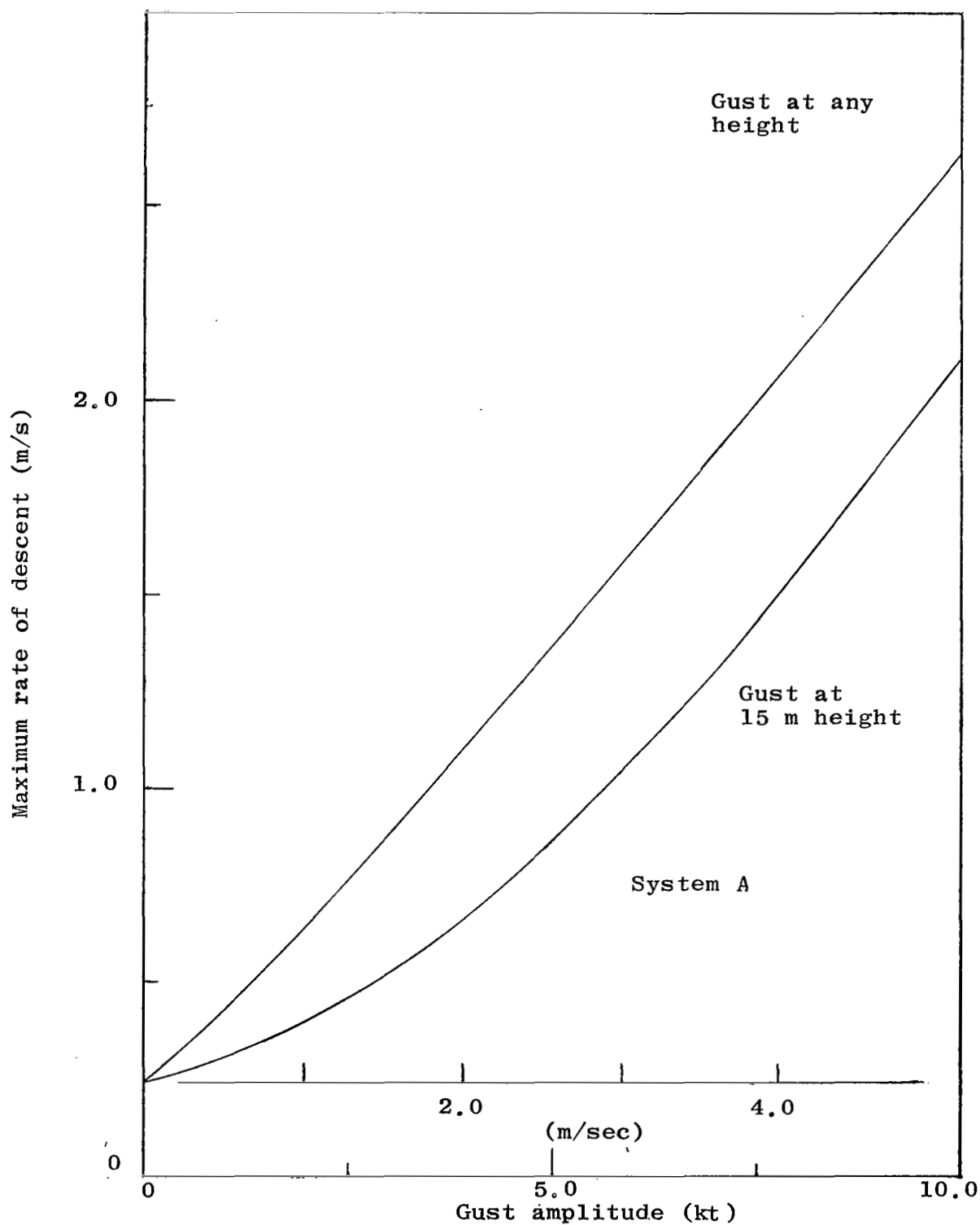to 0.6 m/s which brackets the tentative FAA maximum descent

Figure 21.   Variation of Touch-Down Rate of Descent.
Head Wind Gusts, Any Duration (Ref. 19).

59

rate of 0.9 m/s [20].

Wind Shear

The local wind shear encountered along the STOL flight path is shown in Figure 22. Severe gradients which change sign near the front of the ellipse are observed. For comparison purposes, the shear along a 6 degree glide slope in a wind over natural, homogenous terrain (i.e., in the up-stream, logarithmic wind profile) is also shown.

The influence of spatially varying wind shears on aircraft stability has not been investigated in general form, however, studies of uniform wind shear (linear wind profiles) are reported in [21, 22, 2]. Figure 23, from Etkin [21] shows the effect of constant wind shear on phugoid roots and short-period roots for a STOL airplane. The range of wind shear from +0.30 to -0.30 $\sec^{-1}$ is covered in the figure, which it should be noted, does not encompass the full +0.40 to -0.50 $\sec^{-1}$ range which would be encountered passing over the semi-ellipse.

The effect of wind shear on the phugoid and pitching modes are seen to be large. A strong positive shear decreases both the frequency and damping of the phugoid, and a strong negative shear changes the real pair of pitching roots into a complex pair representing a pitching oscillation of long period and heavy damping. The time the air-craft is in the disturbance is short compared to the phugoid period and hence the phugoid oscillation is unimportant.
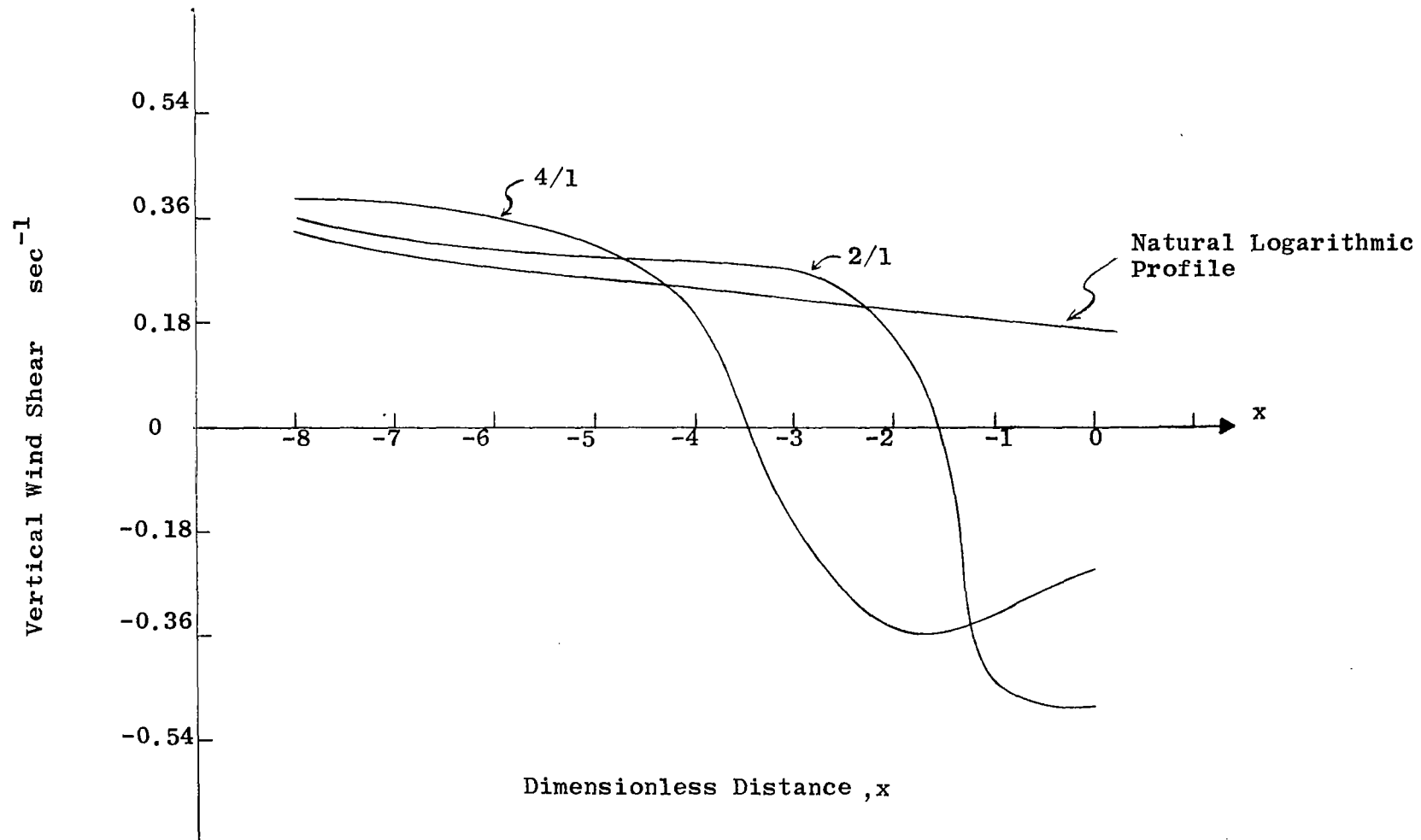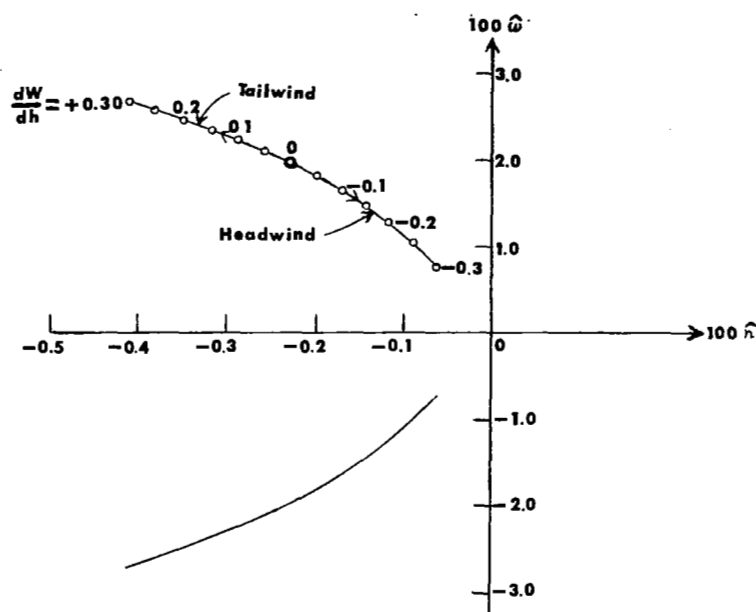
Figure 22.   Wind Shear Encountered By STOL Aircraft

$\hat{\omega}$ and $\hat{n}$ are nondimensional
eigenvalues of the
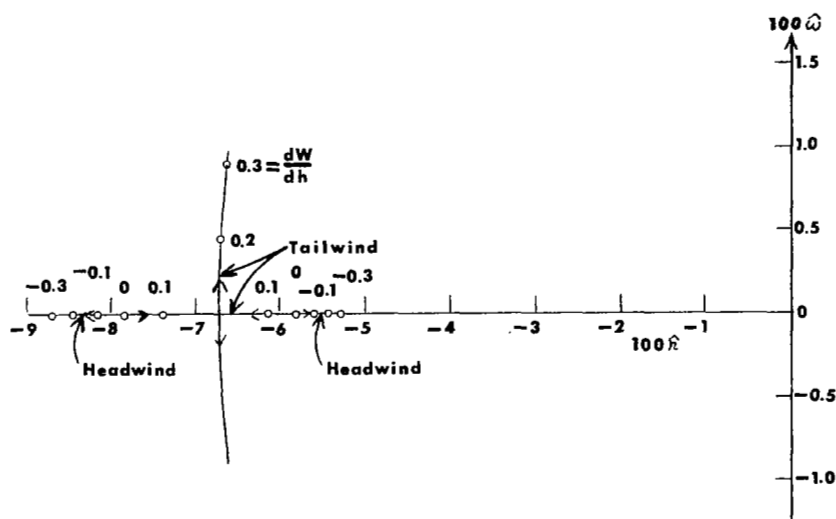characteristic equation
of motion

Figure 23.   Effect of Wind Shear on (a) Phugoid Roots;
             (b) Short Period Roots--STOL Aircraft
             (Ref. 21).

However, the pitching oscillations would be significant. These effects could become large in the disturbed wind over the semi-ellipse. It should be noted that the analyses of [21] assumes the aircraft continuously experiences shear, whereas the shear discussed here is highly localized.

Gera [22] carried out a similar analysis to Etkin [21] and found that for his particular airplane an unstable root appears for wind shears of 0.183 $\sec^{-1}$. He concludes that for certain configurations and flight conditions the appearance of this diverging first-order root may be important and may warrant careful analysis.

Conclusions

The preceding section has described the computed flow fields in context with aircraft operations. Comparisons are made with other reported analyses and experiments based on idealized models of both the flow fields and the airplane dynamics, however, the following conclusions are warranted. In all the comparisons made the magnitude of the winds computed in this study along the 6 degree STOL flight path are on the order of wind conditions considered adverse by other investigators. This is not the case for CTOL aircraft because of the less steep flight path, 3 degrees.

The recommended 15:1 obstruction clearance surfaces [17] for STOL ports in urban areas, therefore, appear perhaps questionable in view of the fact that wind disturbances created by semi-elliptical terrain regularities extend into

the clear region sufficiently far to generate wind environ-
ments which are boarder-line for safe operations. Addi-
tionally bluff bodies and trailing wakes behind surface
proturbances will create even stronger wind disturbance than
the smooth curved ellipse, although, three dimensionality
will tend in some cases to alleviate these disturbances.

No attempt has been made here to conduct an extensive
parametric study of wind speeds, surface roughness, aspect
ratio, etc. on the airplane performance. Rather an effec-
tive tool embodied in the computer code for modelling the
disturbed wind field is presented which can be used to
conduct a more generalized study. In view of the apparent
closeness of the wind environment over an elliptical surface
to boarder-line hazardous flight winds, careful appraisal of
current thinking on 6 degree glide slopes and 15:1 obstruc-
tion clearance surfaces seems necessary and further investi-
gation along these lines is being continued.

CHAPTER X

CONCLUSIONS

The boundary layer analyses presented herein of flow over a semi-elliptical surface obstruction using the turbulence kinetic energy equation leads to the following conclusions:

1. The Prandtl mixing length model and turbulence kinetic energy equation model predict essentially the same velocity profiles for the boundary layer analysis of flow over a semi-elliptical surface. Slight variations in the wind profiles occur in the region of varying pressure gradient due to the diffusion and convection properties of the turbulence kinetic energy inherent to the TKE model and absent in the PML model. It is believed for this reason the TKE model gives somewhat better velocity prediction than the PML model.

2. A region of high turbulence intensity occurs above the stagnation point at approximately the height of the semi-ellipse and a sharp gradient in intensity appears along a line where transition from adverse to favorable pressure gradient takes place.

3. The same conclusions are made regarding the influence of surface roughness and ellipse aspect ratio on maxima in wind speed upstream separation

65

bubble and velocity profiles as were drawn for the PML model and stated earlier on page 3 of this paper.

4. The code developed in this study provides an effective tool for investigating the influences of a wind disturbed by a terrain irregularity on the flight operations of aircraft. Interpretation of the computed flow fields over the semi-elliptical surface suggests that the 15:1 obstruction clearance and 6 degree glide slope presently recommended for STOL aircraft may be inadequate for saft flight operations.

LIST OF REFERENCES

67

LIST OF REFERENCES

1. McManus, R. M. P. "Experience with a Low Altitude Turbulence Model for Autoland Certification," AGARD-CP-140, 1973.

2. Glaser, J. J. "Data Requirements on Turbulence in the Earth's Atmospheric Shear Layer for STOL Design Criteria," AGARD-CP-140, 1973.

3. Ramsdell, J. V., and D. C. Powell. "Meteorological Information for Vertical and Short Take-Off and Landing (V/STOL) Operations in Built-Up Urban Areas--An Analysis," FAA-RD-72-137, 1973.

4. Frost, W., J. R. Maus, and W. R. Simpson. "A Boundary Layer Approach to the Analysis of Atmospheric Motion Over a Surface Obstruction," The University of Tennessee Space Institute, Tullahoma, 1972.

5. Byrne, William M., Jr. "Use of the Turbulence Kinetic Energy Equation in Prediction of Nonequilibrium Turbulent Boundary Layers." Ph.D. dissertation, University of Missouri, Rolla, 1970.

6. Lee, S. C., and P. T. Harsha. "The Use of Turbulence Kinetic Energy in Free Mixing Studies," AIAA Journal, No. 6, 8:1026-1032, 1970.

7. Bradshaw, P., D. H. Ferriss, and N. P. Atwell. "Calculation of Boundary Layer Development Using the Turbulent Energy Equation," Journal of Fluid Mechanics, Part III, 28:593-616, 1967.

8. Fichtl, G. H. "Problems in the Simulation of Atmospheric Boundary Layer Flows," AGARD-CP-140, 1973.

9. Harsha, P. T. "Free Turbulent Mixing: A Critical Evaluation of Theory and Experiment." Ph.D. dissertation, The University of Tennessee, Knoxville, 1970.

10. Townsend, A. A. The Structure of Turbulent Shear Flow. Cambridge: Cambridge University Press, 1956.

11. Byrne, William M., and Shen C. Lee. "A Differential Method for the Prediction of the Effects of Atmospheric Boundary Layer Turbulence Using the Turbulence Kinetic Energy Equation," Proceedings of the Symposium on Air Pollution, Turbulence, and Diffusion, December 7-10, 1971, March 1972. Pp. 231-243.

12. Dutton, J. A., and G. H. Fichtl. "Approximate Equations of Motion for Gases and Liquids," Journal of Atmospheric Science, 26:241-254, 1969.

13. Jackson, P. S., and J. C. R. Hunt. "Turbulent Wind Flow Over a Low Hill," to be published in Journal of Fluid Mechanics.

14. Launder, B. E., and D. B. Spalding. Mathematical Models of Turbulence. London: Academic Press, 1972.

15. Robertson, J. M., and D. B. Taulbee. "Turbulent Boundary Layer and Separation Flow Ahead of a Step," Developments in Mechanics, Vol. 5, 1969.

16. Criteria for Determining Obstructions to Air Navigation. U.S. Civil Aeronautics Administration, Technical Standard Order N-18.

17. Planning and Design Criteria for Metropolitan STOL Ports. Federal Aviations Administration, AC 150/5300-8, U.S. Department of Transportation, 1970.

18. Neuman, F., and J. D. Foster. "Investigation of a Digital Automatic Landing System in Turbulence," NASA TN D-6066, 1970.

19. Corbin, M. J., and K. F. Goddard. "The Design of Automatic Flight Control Systems to Reduce the Effects of Atmospheric Disturbances," AGARD-CP-140, 1973.

20. Tentative Airworthiness Standard for Powered Lift Transport Category Aircraft. Federal Aviations Administration, U.S. Department of Transportation, 1970.

21. Etkin, B. Dynamics of Atmospheric Flight. New York: John Wiley and Sons, 1972.

22. Gera, Joseph. "The Influence of Vertical Wind Gradients on the Longitudinal Motion of Airplanes," NASA TN D-6430, 1971.